METALORGANIC CHEMICAL VAPOR DEPOSITION AND INVESTIGATION OF ALGAINN MICROSTRUCTURE

by

Jonathan W. Anderson, B.S.

A thesis submitted to the Graduate Council of
Texas State University in partial fulfillment
of the requirements for the degree of
Master of Science
with a Major in Physics
August 2014

Committee Members:

Edwin L. Piner, Chair

David Donnelly

Mark W. Holtz

FAIR USE AND AUTHOR'S PERMISSION STATEMENT

Fair Use

Duplication Permission

DEDICATION

To my parents

ACKNOWLEDGEMENTS

First and foremost, I must thank my adviser Dr. Edwin Piner for introducing me to MOCVD and the III-nitrides, and for providing so many interesting research opportunities. I would like to thank my committee members Dr. David Donnelly and Dr. Mark Holtz for taking the time to review this work and for their feedback. I would also like to thank Dr. Kyoung-Keun Lee for all his help in making the reactor operational.

Special thanks must be extended to Dr. Arturo Ponce-Pedraza and Dr. Francisco Ruiz-Zepeda at the University of Texas at San Antonio for teaching me about STEM and for their excellent microscopy work, and to IQE for providing the AlGaInN sample studied.

Finally I would like to thank my family, who have supported me in all of my endeavors.

TABLE OF CONTENTS

Page

LIST OF FIGURES

Figure **Page**

ABSTRACT

The group III-nitride family of semiconductor materials grown by metalorganic chemical vapor deposition (MOCVD) has had a dramatic impact on optoelectronics and high-frequency, high-power devices in recent years. The nitrides possess wide, direct transition band gaps ranging from 6.2 eV for AlN to 3.4 eV for GaN to 0.9 eV for InN which has allowed the development of LEDs and laser diodes in the blue and UV spectrum. Furthermore, the band gap, combined with a high electron saturation velocity and the piezoelectric properties of the (AlGaIn)N/GaN interface allow for the formation of a two-dimensional electron gas which can be utilized to produce high electron mobility transistors (HEMTs).

To date most research has focused on AlGaN/GaN heterostructures, which have proven extremely useful for HEMTs but less than ideal for UV LEDs. The quaternary AlGaInN has emerged as an alternative to AlGaN that promises to further enhance HEMT performance and produce better quality UV LEDs. However, the addition of In to the alloy can be problematic because it is not completely soluble and tends to form clusters through spinodal decomposition. Studies of phase separation in AlGaInN have been made, but have focused on films composed mostly of Ga. Recently, HEMTs made using a high Al content AlGaInN layer have shown comparable performance to devices made using AlGaN, but no studies of phase separation have been done on these high Al content films.

In this thesis, the installation of a MOCVD reactor at Texas State University and the modifications necessary to make it operational will be presented. Furthermore, the progress made in developing of processes to deposit AlGaN/GaN heterostructures will also be discussed. Finally, evidence of phase separation by

spinodal decomposition in a sample of high aluminum content AlGaInN, provided by IQE, from a study by scanning transmission electron microscopy in collaboration with the Yacaman group at the University of Texas as San Antonio will be presented, and the results discussed within the context of the regular solution model.

CHAPTER 1

Introduction

Chemical vapor deposition (CVD) has become an indispensable tool for the epitaxial growth of thin films which are necessary to produce modern semiconductor devices. Epitaxial growth occurs when a single-crystal thin film is grown on a single crystal substrate.[1] In a CVD process precursor materials containing the elements to be included in the deposited film are brought into a reaction chamber where they decompose and adhere to a substrate. The chemical reactions that occur between the substrate and the precursor materials can become quite complex in contrast to physical deposition methods that rely on plasma sputtering or evaporation. The first implementation of a CVD process has been traced back to 1855,[1] when it was used to deposit tungsten. Since then, CVD processes have been developed to deposit a variety of metals as well as III-V and II-VI compound semiconductor materials.[1,2] In order to produce different materials, several variations of CVD have been developed, typically distinguished by the precursors used, such as plasma enhanced CVD, atomic layer deposition, hydride vapor phase epitaxy (HVPE), and metalorganic chemical vapor deposition (MOCVD). This work will focus on the use of MOCVD and its application to produce III-nitride materials.

Theoretical research on the properties of III-V semiconductors had begun in the 1930s but experimental results did not appear until the late 1960s when epitaxial techniques, including MOCVD, had developed to the point that material of sufficient quality could be produced.[3] Experimental research into the III-nitrides began in the 1930s as well when powder samples were synthesized which led to the determination of their structural properties by x-ray diffraction.[4] After this initial period of interest, little research was focused on the III-nitrides until they received renewed

interest in the 1970s based on the success of the other compound semiconductors such as GaAs and InP that had recently been produced. The first report of GaN being grown by CVD came in 1969 by Maruska using HVPE,[5] and in 1971 Manasevit reported growth of AlN and GaN by MOCVD using trimethylaluminum, trimethylgallium and ammonia on sapphire, Si, and SiC substrates.[6] These precursors and substrates still form the basis for modern MOCVD growth processes.

From this early work it was determined that the III-nitrides had wide, direct-transition band gaps ranging from 6.2 eV for AlN to 3.4 eV for GaN to 1.9 eV for InN[4] (high quality InN is difficult to produce, and a more recent study on better quality material determined the band gap to be 0.9 eV,[7] the currently accepted value). This allows the band gap to be tuned by forming alloys to values that cover the infrared to ultraviolet spectrum making the III-nitrides particularly attractive for optoelectronic devices where they have found applications in LEDs, laser diodes,[8] photodetectors,[9] and solar cells.[10]

One of the major challenges encountered while trying to produce device quality material was cracking of the deposited film caused while cooling down from the high growth temperatures caused by the differences in the lattice constants and coefficients of thermal expansion between film and substrate. The lack of native substrates on which to grow the III-nitrides still remains an issue. The first step to growing single-crystal films came in 1985 when Amano found that by first depositing a layer of AlN a crack-free GaN layer could be grown.[11] In 1989 Amano found that p-type doping of GaN could be achieved by doping with Mg using bis-cyclopentadienyl magnesium and then treating the film with low-energy electron-beam irradiation, and then used the material to form a p-n junction from which electroluminescence was observed in the UV region.[12] The demonstration of p-type doping and electroluminescence was a watershed moment in the development of the III-nitrides because of the enormous commercial markets for LEDs and laser

diodes at short wavelengths that cannot be achieved commercially using other materials.

In 1992 Matsuoka was able to overcome the difficulties associated with working with In containing compounds to produce the first InGaN material from which photoluminescence spectra could be observed, and also produced the first samples of AlGaInN[13]. The first samples of AlGaInN were polycrystalline and single-crystal AlGaInN was not produced until 1996.[14]. The reason III-N materials containing In are difficult to produce is due to the much higher equilibrium vapor pressure of nitrogen over InN compared to AlN or GaN. If sufficient nitrogen is not available during growth In droplets form and evaporate, limiting the amount of In that is incorporated into the alloy. This creates a situation where the high temperatures needed for good crystal quality must be sacrificed to promote In incorporation.[13] These are issues that affect any nitride alloy containing In. To better understand the relationship between temperature and composition the thermodynamics of the InGaN system were modeled using the regular solution model[15], and its results confirmed by experiment.[16] An extension of the regular solution model has also been applied to AlGaInN,[17,18].

InGaN/GaN heterostructures became the basis for blue LEDs, but in order to develop LEDs in the UV spectrum the InGaN is replaced with AlGaN because of its wider band gap. However, the high Al content required in the AlGaN layer creates issues. In general it is difficult to grow good quality AlGaN with high Al content and the stress created by the lattice mismatch combined with the piezoelectric properties leads to defects and undesirable electric fields which degrade device performance.[19] In addition to optoelectronic applications, the wide band gap of the AlGaN/GaN heterostructures indicates they should operate well at high temperatures. This, combined with high electron saturation velocities, and large spontaneous and piezoelectric polarizations that can be utilized to form a two-dimensional electron

gas (2DEG),[20] makes them ideal for producing high electron mobility transistors (HEMTs). AlGaN/GaN heterostructures have proven remarkably successful in HEMT applications but in order to further improve performance of HEMTs and UV LEDs attention has turned to replacing AlGaN with InAlN or AlGaInN.

InAlN is an attractive alternative that can be grown lattice matched to GaN and can theoretically span the entire range of band gap energies available to the nitrides. Even early devices produced with InAlN showed promising results.[21] However, calculations based on the regular solution model predict single phase material can only be produced in a narrow range of compositions when grown in the 700-800 °C range typically used for growth by MOCVD.[22] While these are the same issues that were encountered with InGaN they are predicted to be more pronounced in InAlN.[18]

The quaternary AlGaInN has the advantage of an additional degree of compositional freedom which allows its band gap and lattice constant to be adjusted independently. Calculations based on the regular solution model indicate that it should be possible to produce single phase material over a larger range of compositions than InAlN grown at the same temperature.[18]

In 2000 Zhang found that introducing In into AlGaN to form $Al_{0.15}Ga_{0.8}In_{0.05}N$ which substantially improved the luminescence of quantum well structures as measured by photoluminescence,[23] and later that same year Chitnis reported on the production of a LED using AlGaInN.[19] In 2002 Hirayama observed fluctuations in cathode luminescence images which was attributed to electron and hole localization caused by In segregation which had been proposed as a mechanism to explain the enhanced luminescence in AlGaInN.[24] During this time period there were several reports of LEDs being made with peak wavelengths in the 290-340 nm range.[25–27] This research in UV LEDs focused on quaternary materials with high Ga content, similar to those used by Zhang, for which phase separation had been predicted using both the regular solution model[18] and more sophisticated methods.[28] In 2006

experiments to verify these predictions were made on $Al_xGa_{1-x-y}In_yN$ samples with $0.107 < x < 0.146$ and $0.006 < y < 0.131$ using Raman spectroscopy, high resolution x-ray diffraction, and transmission electron microscopy.[29]

There are fewer reports on quaternary HEMTs available. In 2004 Liu demonstrated Schottky contacts to AlGaInN, which are necessary for HEMTs, and observed the formation of a 2DEG.[30] These results were extended in 2005 by producing a transistor.[31] Studies have been done on the variation of electrical properties with alloy composition finding that generally the quaternary samples had comparable sheet charge density and higher carrier mobility than found in InAlN/GaN heterostructures but were unable to match the mobility of AlGaN/GaN structures.[32,33] In 2013 devices were produced using high Al content quaternaries that demonstrated a carrier mobility of 2200 $cm^2\,V^{-1}\,s^{-1}$at 40 GHz,[34] comparable to AlGaN devices, and showed record-high cutoff frequencies f_T/f_{max} of 230/300 GHz.[35]

In summary, MOCVD and the III-N materials are inextricably linked. This thesis is divided into two parts which cover both subjects. In chapter 2 the major components of a MOCVD reactor are discussed as well as how they are used in the reactor at Texas State University. Chapter 3 will discuss the development of AlN, GaN, and AlGaN processes using the reactor. Chapter 4 will discuss an investigation into the microstructure of a high Al content AlGaInN sample by scanning transmission electron microscopy to determine to what extent phase separation is occurring. Finally, chapter 5 will provide insight into future work, and conclusions.

CHAPTER 2

Metalorganic Chemical Vapor Deposition

This chapter covers the principles of MOCVD reactor design with an emphasis on the use of a cold wall, vertical rotating disk reactor to deposit III-nitride materials. First the basic components that comprise a MOCVD reactor will be discussed, followed by a description of how these components are used in the reactor at Texas State University. The installation and modifications that were necessary to make the reactor operational will also be discussed.

2.1 Principles of MOCVD

The basic goal of MOCVD is to bring precursor materials into a reaction chamber where they are evenly distributed over a substrate and decompose via pyrolysis to form a uniform epitaxial layer. The most commonly used source of nitrogen for the III-nitrides is anhydrous ammonia, which is a liquid but has a sufficiently high equilibrium vapor pressure at room temperature that it can be delivered directly to the reaction chamber as a gas.

The situation is more complicated for the organometallic (OM) species. The most commonly used OM sources are trimethylaluminum (TMA), trimethylgallium (TMG), and trimethylindium (TMI). At room temperature TMA and TMG are liquids and TMI is solid, which prevents them from being delivered directly to the chamber. All three come in sealed metal containers, known as bubblers, because of their pyrophoric nature. Extreme care must be taken to ensure that there are no leaks in the connections between the bubblers and the reactor and that all oxygen has been purged from the lines before opening them. To get the OM materials to the reactor, a carrier gas is flowed into the bubblers where it enters through a dip

tube submerged in the OM. After "bubbling" through the liquid OM, the carrier gas becomes saturated with the vapor phase OM that exists above the liquid and carries it into the reactor. The amount of OM delivered into the reactor depends on the equilibrium vapor pressure and typically is on the order of micromoles. The flow rate of OM material in moles/minute out of the bubbler can be calculated as[1]

$$M_{OM}\ (\text{mol/min}) = \frac{F_C\ (\text{sccm})}{22,400\ (\text{cm}^3/\text{mol})} \times \frac{P_V}{P_T - P_V} \tag{2.1}$$

where F_C is the flow rate of the carrier gas, P_T is the total pressure above the OM, and P_V is the vapor pressure of the OM. The vapor pressure can be modeled for a particular material at absolute temperature T using the parameters a and b by the equation[2]

$$\log(P_V) = a - b/T. \tag{2.2}$$

The exponential temperature dependence of P_V requires the bubblers be kept in chilled baths to very carefully and accurately regulate their temperature in order to maintain consistent delivery. The ammonia can be treated as an ideal gas, and the molar flow rate is calculated as

$$M_{NH_3}\ (\text{mol/min}) = \frac{F_{NH_3}\ (\text{sccm})}{22,400\ (\text{cm}^3/\text{mol})} \tag{2.3}$$

The ratio M_{NH_3}/M_{OM} calculated from equations 2.3 and 2.1 is referred to as the V/III ratio and is almost always listed in literature describing growth processes because it is an important parameter in determining the properties of the deposited material. It should be noted that the V/III ratio necessary for a particular process is reactor dependent and the values listed in literature may only be useful as a starting point for developing a process. Hydrogen is the preferred carrier gas because of the high purity that can be achieved using a palladium cell to minimize impurities incorporated into the film, although in principle any inert gas can be used. However, it is important to note that nitrogen that has been passed through a

chemical purifier is typically used for processes involving indium because hydrogen has a highly negative impact on indium incorporation.[36]

The hydrogen, nitrogen, and ammonia are stored in gas cylinders at high pressures that are reduced by pressure regulators before they connect to the system. From there flow through the system is controlled electronically using a system of thermal mass flow controllers (MFCs), pressure controllers, and pneumatic valves. A MFC consists of a main flow cavity through which the flow is regulated using an electronically controlled valve. A small portion of the flowing gas is siphoned into a capillary tube from the main cavity with two heated temperature sensors. Based on the temperature change of the sensors in the capillary tube caused by the flowing gas the flow rate can be determined from the equation

$$q = FC_p\Delta T \tag{2.4}$$

where q is the heat lost, F is the flow rate, C_p is the heat capacity, and ΔT is the change in temperature. With this information the control electronics adjust the position of a valve to match the flow to the given setpoint. The dependence of the flow rate calculation on the heat capacity of the gas requires the MFC to be calibrated for a specific gas. In older analog MFCs, this calibration is fixed and if a different gas or mixture of gases is to be used a scaling factor must be calculated. The details of this calculation can be found in documentation from the manufacturer. Newer digital MFCs can be connected to a computer and reprogrammed to change the gas the unit is calibrated for. The maximum flow through a MFC is determined by the cavity sizing and specified when ordering the unit. In general a MFC will flow most accurately near its maximum flow and may not be accurate if the flow rate is set below 20% of its maximum value. Pressure controllers operate in much the same way as MFCs but with the valve controlled by reading from a pressure gauge rather than the thermal sensors found in a MFC.

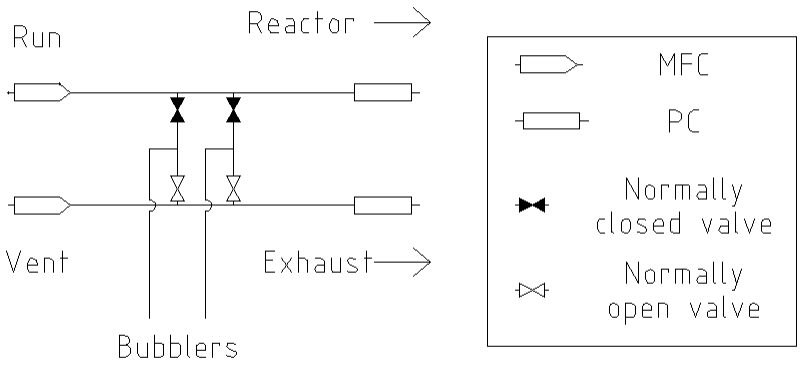

Figure 2.1: Example of a simple vent/run manifold.

In order to create abrupt interfaces between layers it is necessary to be able to rapidly switch the flows from the bubblers into the reactor on and off. This is done by linking a normally closed valve to a normally open valve in a configuration known as a vent/run manifold illustrated in figure 2.1. Flow is started in the vent line which bypasses the reactor, and when required, the valves are activated diverting the flow to the reactor. Flow rates through the bubblers into the manifold are low, typically less than 200 sccm, so a second MFC with a higher flow rate is placed on the line upstream of the valves to provide gas to push the OM material to the chamber quickly, and to provide sufficient flow rate so that the flows into the reactor chamber can be tuned for uniformity across the wafer. Pressure controllers are placed down stream of the manifold to balance the pressure between the vent and run lines to prevent a pressure surge when the valves are activated.

The reactor chamber body consists of three main parts: a top plate that the gases enter through which is designed to disperse the precursors across the substrate, the chamber side walls, and a bottom plate. The bottom plate has the electrical feedthroughs for the connections to the heater, a rotational feedthrough

that links a shaft to a motor outside the chamber, and exhaust connections to the system pump. All three of these pieces are water cooled to prevent damage from the high temperatures used in deposition.

Inside the chamber the substrate is supported on a susceptor that sits on the motor shaft above the heater and is rotated to help deposit the film uniformly. Typically susceptors are made from SiC coated graphite. Graphite provides a low cost, easily machinable material that has a high thermal conductivity. SiC is used as a coating because it provides a chemically inert surface that prevents carbon contamination of the film during deposition, and the coefficient of thermal expansion of SiC can be matched with graphite to prevent it from delaminating during heating and cooling. The heater temperature is controlled by a thermocouple and the surface temperature of the substrate is monitored by a pyrometer to ensure deposition occurs at the proper temperature. The difference in temperature as measured by the pyrometer and thermocouple can be several hundred degrees because of the distance from the element and the cooling provided by the carrier gases.

A process pump and throttle valve are used to regulate the pressure inside the chamber which can impact the flow dynamics in the chamber and the quality of the material produced. Typically, the chamber pressure during deposition is between 50-760 torr depending on the design of the reactor. At these pressures many of the maintenance issues associated with the ultra high vacuum systems necessary for sputtering or molecular beam epitaxy systems, such as baking out the system, are avoided. However, the higher pressures also mean that in situ characterization techniques that require ultra high vacuum conditions, such as RHEED, cannot be used.

The final major component of a MOCVD reactor is the loading system. This consists of a load lock separated from the main chamber by a gate valve that can be

pump-purged with nitrogen to remove any oxygen before loading the wafer into the main chamber via a transfer arm or to remove any reactants that may have gotten into the load lock during unloading before opening it.

2.2 Texas State University III-Nitride MOCVD Reactor

The schematics in figures 2.2, 2.3, and 2.4 were created as the modifications that will be discussed in the next section were being made and show the current configuration of the reactor at Texas State. As previously discussed hydrogen, nitrogen, and ammonia are delivered in high pressure cylinders. The hydrogen and ammonia cylinders are stored in vented gas cabinets for safety. All cylinders are connected to regulators that reduce the pressure from the cylinder pressure, which is 2400 psi for full hydrogen and nitrogen cylinders. From there the gases, with the exception of hydrogen, pass through chemical purifiers and a second set of regulators further reduces the pressure. The hydrogen purifier is currently being bypassed because of contamination issues that will be discussed later. The purifiers the gas cabinets are connected to are seen at the bottom of figure 2.2. From there the gases are split into two branches: the hydride lines which deliver the ammonia and the alkyl lines which deliver the OMs.

As would be expected from the discussion in the previous section, the hydride branch, shown highlighted in blue in figure 2.2, is the simpler of the two. After passing through the regulators on the reactor, the flow of each gas is controlled by a MFC which feeds into a vent/run manifold. This allows any combination of gases to be delivered to the chamber.

The hydrogen and nitrogen lines are split to connect to the alkyl branch, highlighted in red in figure 2.2, where pneumatic valves allow one or both of the gases to flow into the reactor. There is a line with a manual valve, which is normally closed, that connects the nitrogen to the ammonia line that can be used to flush the

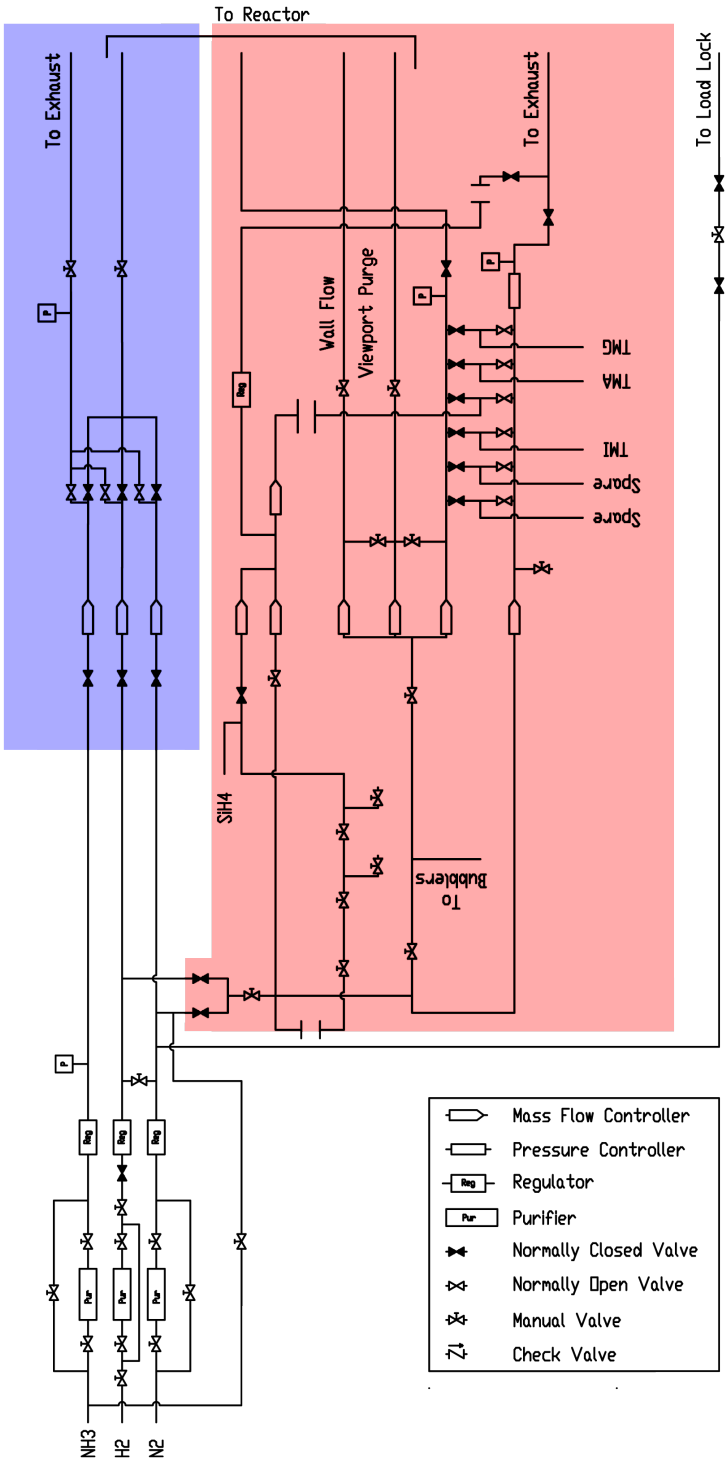

Figure 2.2: Schematic showing the reactor gas delivery system. Hydride lines are highlighted in blue and alkyl lines in red.

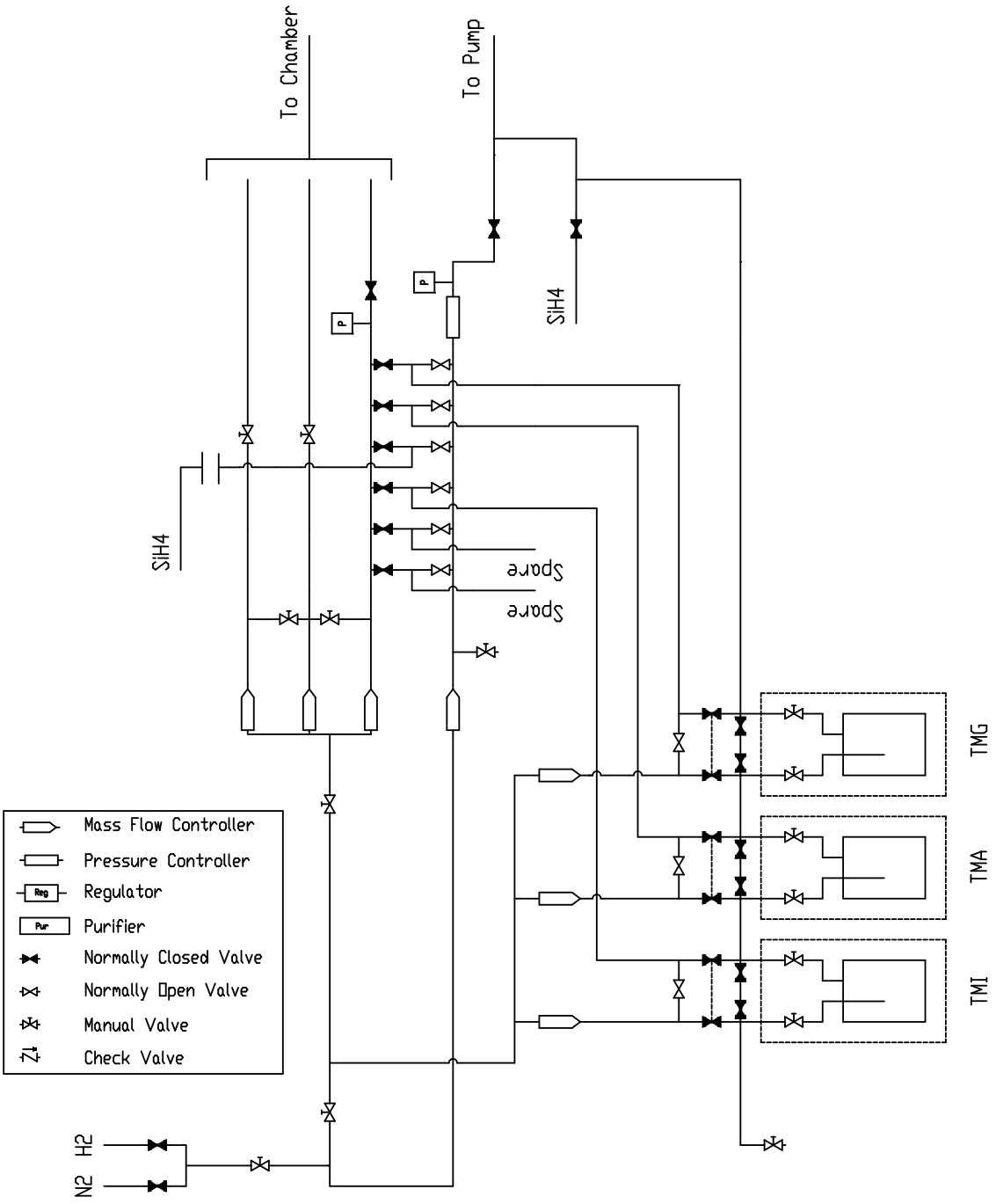

Figure 2.3: Schematic showing the organometallic bubbler connections to the reactor.

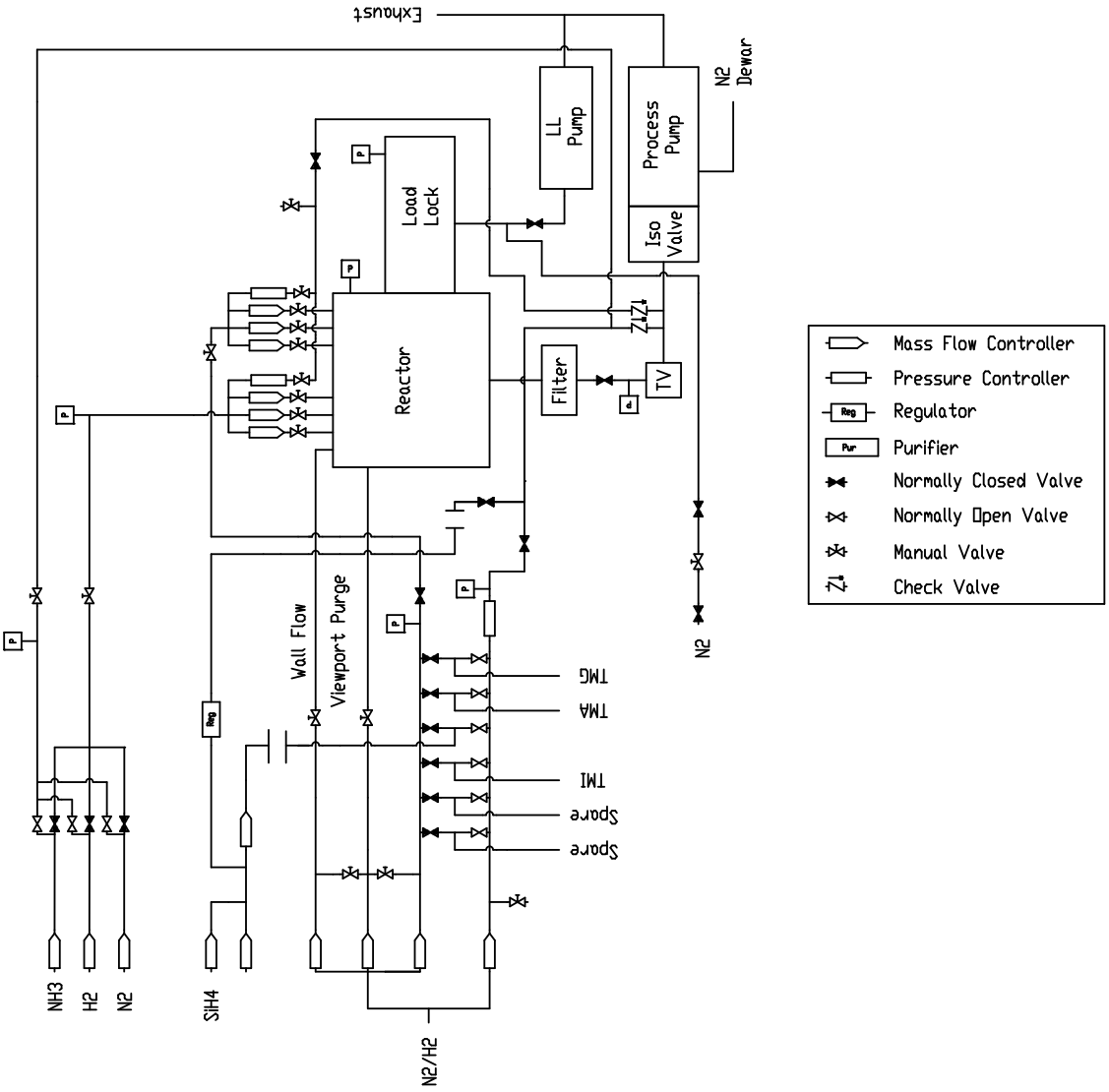

Figure 2.4: Schematic showing connections to the reaction chamber.

ammonia line which is needed to change the purifier. Alternatively, nitrogen can be flowed directly through the ammonia line from the gas cabinet. After the pneumatic valves the gases feed the lines for the vent/run manifold for the OMs.

The run line splits two more times. The first split provides the push gas for the bubblers as can be seen in figure 2.3, which shows a view of the bubbler connections in detail. Flow into the bubbler is regulated by an MFC which feeds into a manifold composed of a normally open valve which by passes the bubbler and two normally closed valves on the bubbler inlet and outlet. These inlet and outlet valves are connected together pneumatically so that if one is open, both must be open to prevent the bubbler from pressurizing. The dashed box around the bubblers indicates what comprises the bubbler separate from the reactor. The second set of valves that connect the inlet and outlet lines between the bubbler and inlet/outlet valves are used for leak checking and pump-purging the bubbler connections and must be activated manually. Pump-purging is done by temporarily making a connection from the nitrogen cylinder to the manual valve near the bubblers and using the system pump.

The second split provides gas directly to the chamber through the view port purge, which flushes material away from the chamber view ports and gate valve, and the wall flow. From the bubblers the OMs enter the alkyl vent/run manifold which has connections for up to six materials. Currently only the TMG and TMA connections are being used with one connection reserved for a silane line that is currently disconnected and another for TMI. This leaves two connections available for future use.

In figure 2.4 we see how the gas delivery systems connect to the reactor chamber. The run lines from both the hydride and alkyl lines connect to a bank of three injector MFCs and a pressure controller, which are all in parallel. Each of the injectors is controlled independently and feeds a separate zone of a diffuser plate at

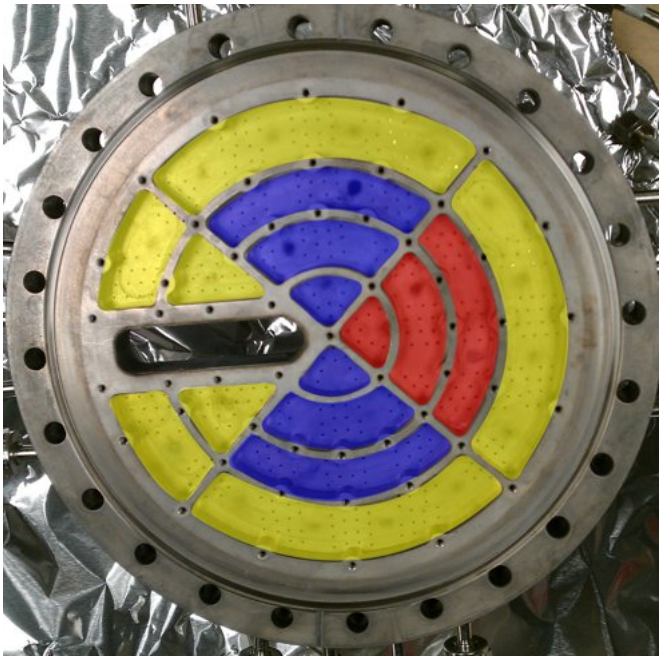

Figure 2.5: Reactor top plate injector zones. The hydride zones are in marked in blue, alkyl in red, and the wall flow in yellow.

the top of the chamber which is seen in figure 2.5. The hydride lines are split between the injector and the top plate of the chamber to feed two zones that are marked in blue if figure 2.5. The precursors are delivered into the chamber using different lines to prevent any unwanted reactions from occurring prior to deposition. The wall flow enters through the outer most zones of the injector plate, and is used to keep the reactants away from the chamber walls to prevent the walls from becoming coated which can change the thermal profile of the reactor and become a source of unwanted particles. At this point the challenge becomes balancing the flows through the different zones, the pressure in the reactor, the rotation rate of the substrate, and the heater temperature to produce high quality materials of uniform thickness and composition with minimal particulates. After leaving the chamber, the exhaust passes through a filter that collects the by products that form from decomposing the OMs and is then passed through the system pump into the building exhaust system.

2.3 Reactor Installation and Modifications

The reactor was donated to Texas State by TriQuint Semiconductor and originally was an early 1990s Emcore design for GaAs growth that had been significantly modified. The system arrived at Texas State in three sections: the gas delivery system, the reactor chamber and load lock, and the control electronics. Installation began in fall of 2011. The first steps were to connect all the process lines between the cabinets, make the connections for the electronics, and wire the system to the main power supply. During this process a new gate valve and load lock were installed to extend the system's capabilities to handle 150 mm wafers and the two gas cabinets for the hydrogen and ammonia that were donated by Texas Instruments were installed.

Originally, both cabinets had space for two cylinders, each connected to separate control panels, but because of the high rate of hydrogen usage the two cylinders in the hydrogen cabinet were connected to one panel and a third gas cabinet installed next to it that houses three cylinders that were connected to the other control panel. This reduces the frequency of cylinder changes and thus the chances for contamination to enter the system. For safety, ventilation ducting was installed connecting the gas cabinets to the building exhaust system.

Prior to arrival, the system had sat idle for some time so it was necessary to test the hardware to ensure everything was operating properly. The initial inspection involved checking for leaks using a Pfeifer Vacuum Smart Test helium leak detector as well as verifying the pneumatic valves and mass flow controllers were operating properly. This proved difficult because of poorly placed leak ports on the system and the detected leak rate was usually on the order of 10^{-7} torr l/s and there were several sections from the previous modifications that were difficult to thoroughly check. The control software that came with the reactor was an archaic MS-DOS program for which we had limited documentation further complicating the testing.

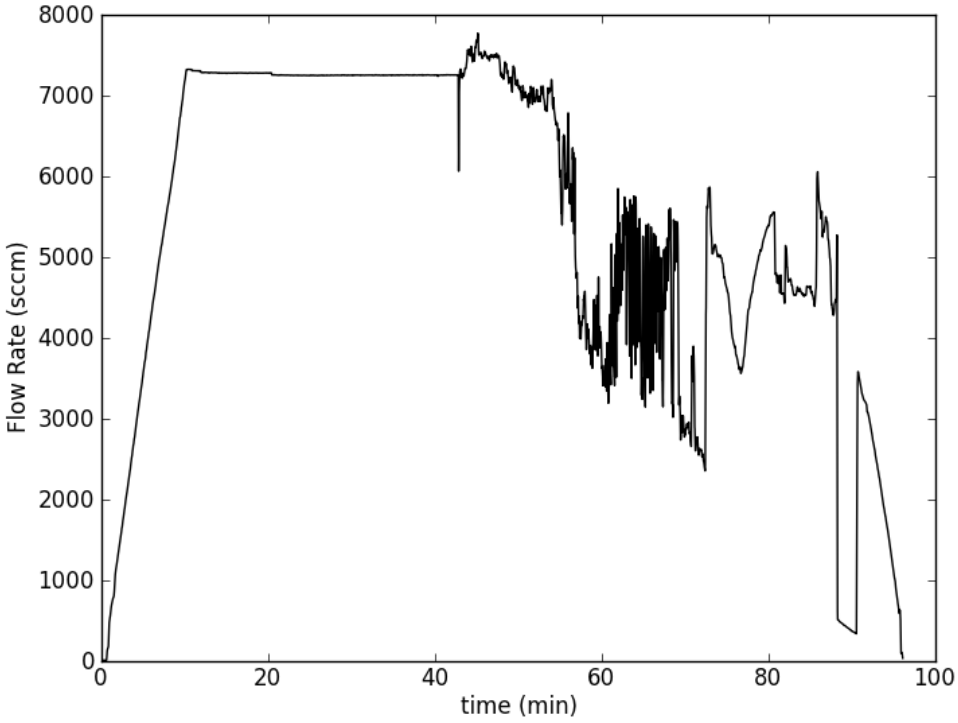

Figure 2.6: Outer alkyl injector showing signs of contamination during a run.

To overcome the limitations of the old control software a new control system was purchased, installed and the hardware was again verified to be in proper working condition in early 2012.

With this system configuration we were able to begin developing processes for depositing AlN, but these initial attempts were plagued with issues. The first runs were performed using 150 mm wafers which broke before deposition began due to temperature variations across the wafer. To address this we began using 1 mm thick wafers and reducing the heating rate at the beginning of the run. These first runs were of mixed success; we were able to deposit material but there were near constant system issues that required us to take the system down for repair.

Issues would first be noticed as instabilities in the flow of the MFCs feeding the alkyl zones, typically problems would first be noticed in the MFC feeding the outer zone as it has the highest flow rate causing it to become contaminated the quickest.

Figure 2.6 shows the flow rate through the outer alkyl injector over the course of a run in which contamination occurred. The flow starts out smooth and controlled until near the 40 minute mark where there is a brief drop in flow that occurred when the vent/run manifold switched sending TMA to the chamber. The drop in flow was caused by a pressure imbalance between the vent and run lines which resulted in a surge in flow when the valves switched. Immediately after the switch occurs the contamination causes the flows to become unstable. Adjusting the setpoint of the MFC somewhat stabilized the flow, this can be seen occurring at 70 minutes, but the MFC was still not controlling.

Upon opening the connections to the injectors a white powder was found around the MFCs. Analysis of the powder by EDS confirmed that it was aluminum oxide, which forms when the TMA encounters an oxygen source such as a leak in a connection. The rapid fluctuations and gradual decrease in flow seen in 2.6 are both indicative of a MFC that has been coated with aluminum oxide powder, and it was also common to see the flow completely stop. There were several cases of such contamination occurring, and it was thought that poor mounting of the alkyl injector MFCs made it difficult to make a leak-tight connection because the powder was typically localized around the injectors. However, after one such incident we found evidence of contamination all the way back to the vent/run manifold. At this point it was decided that a complete overhaul of the system was necessary in summer 2012.

The first step in the overhaul was to remove all of the unused portions of the system and in doing so it was found that many of the lines had been heavily coated with unknown materials, seen in figure 2.7. Previously the system was constructed using 0.25 in stainless steel tubing and a combination of VCR and microflange connections. The microflange connectors are a rather awkward design which requires three screws to be tightened around a collar to form a seal. The problem

Figure 2.7: Contamination found in lines during system overhaul.

with this becomes apparent when trying to secure one of these connections in a tight space and there is not enough room reach all of the screws. Many of the connections we removed were questionably secure. Thus, the lines were replaced and as many connections as were reasonably possible were converted to VCR.

While the lines were being replaced new manual valves and leak ports were installed. These allow for isolating smaller sections of the system to reduce the time required for leak checking and allow for checking to a leak rate of at least 10^{-9} torr l/s, compared to the 10^{-7} torr l/s that was previously achievable.

The previous vent/run manifold was made out of a single metal block where the lines from the bubblers fed into, and the gases mixed before being delivered to the chamber. The main drawback of this design is that it is nearly impossible to clean and given the condition of the lines connected to it, and the previously observed aluminum oxide powder, it was likely contaminated and needed to be replaced. A new vent/run manifold was constructed by placing VCR tees between a normally open and normally closed valve whose pneumatic connection had been linked together. Six pairs of these valves were linked together to form the manifold and then mounted to a piece of sheet metal to help maintain their structural integrity.

Previously, the MFCs feeding the alkyl zones of the chamber and their isolation

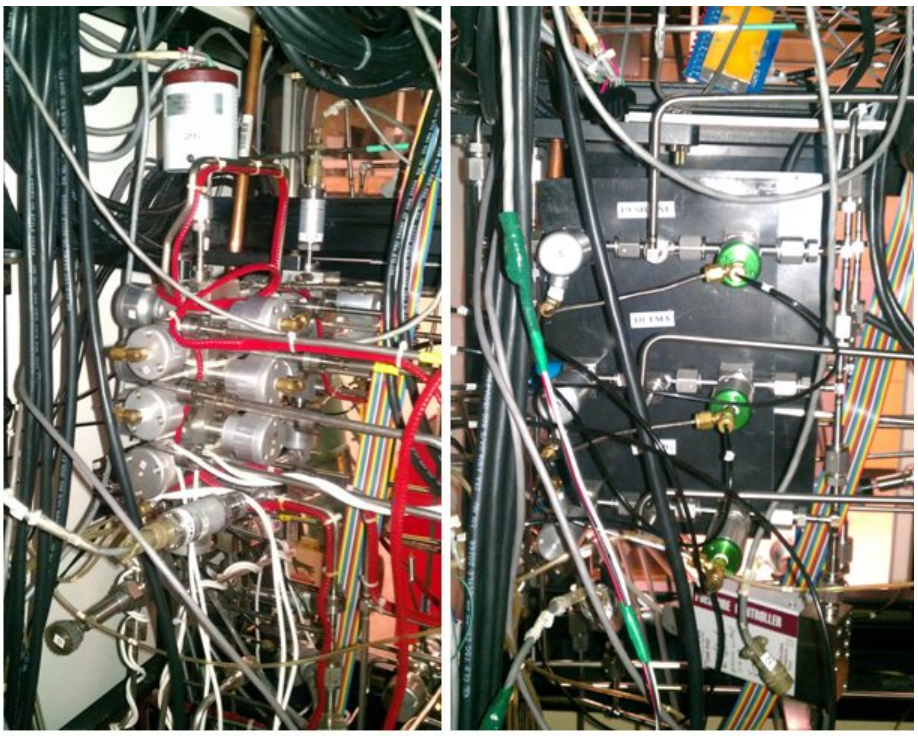

(a) (b)

Figure 2.8: (a) Old vent/run manifold and (b) replacement made during overhaul.

valves had only been supported by the tubing connecting them and had been the cause of many issues. These were mounted next to the hydride MFCs to secure them and new lines were made connecting them to the chamber. While this work was being done the main process pump began to have issues so a new pump was purchased and installed. Pressure controllers were installed to control the pressure in the lines feeding both the alkyl and hydride injectors and on the vent side of the OM vent/run manifold to balance the pressure between the lines to prevent the flow surge seen in figure 2.6. Also, it was found that only two of the three zones of the gas diffuser plate were being used, so the flows from the hydride injectors were split in an attempt to improve the transport of material to the substrate.

All of these made the reactor more stable. In November 2012 we were able achieve our first successful AlN depositions, but we soon were having issues again with oxygen contamination. We were finally able to determine the contamination

was coming from a combination of factors.

First, it was found that the new process pump was not leak tight and allowed air to enter the system when it was shut off. This was likely an issue with the original pump as well. This was addressed by installing an isolation valve on the pump that automatically closes when the power is turned off, installing check valves on the vent lines that connect to the pump, and modifying our shut down procedure to close the valves on the reactor side of the injector MFCs before turning off the pump. This prevents any oxygen from back flowing into the reactor. Second, if contamination does occur and the aluminum oxide powder gets into a valve, it can damage the valve seat causing it to not form a good seal and leak causing other portions of the system to become contaminated. This makes it difficult to determine the source of the contamination. Finally, we suspect the chemical purifiers for the gases that were on the system when we received it were releasing contamination into the system. A chemical purifier removes gas impurities by an exothermic chemical reaction; in testing we found the ammonia purifier would become cool to the touch indicating an endothermic reaction suggesting that it could be outgassing.

After repairing or replacing all contaminated valves, bypassing the original purifiers, and installing the isolation valves on the exhaust line in early 2013 there have not been any more issues with oxygen contamination. As a precaution we replaced the TMA bubbler because of the extent of the contamination, and once the reactor proved stable new nitrogen and ammonia purifiers were installed.

At this point we were able to begin our process development, but soon found that the power supply for the main heater was unable to deliver sufficient power to reach the deposition temperatures needed to grow good quality material. A new power supply was installed in the summer of 2013, but the cooling setup for the diffuser plate was over taxed at the higher deposition temperatures and was limiting the deposition time. To remedy this a new recirculating chiller was installed in fall

of 2013. We also purchased a new pyrometer with better data logging capabilities during this period.

As we began to grow samples more regularly, we began to notice issues with the heater elements. The original heater design consisted of a main heater element sitting on boron nitride rods and a coil of wire inside a cup around the motor shaft, both made of tungsten. The main element heats the substrate while the coil heats the motor shaft to reduce heat loss. This is an unconventional design that leads to variations in temperature across the wafer as measured by the pyrometer. Normally what is the main heater element in our system would be split into multiple independently controlled sections for uniform heating. Another issue with this design is that tungsten reacts with the hydrogen and ammonia causing the heater element to warp, become embrittled, and eventually break. Typically the main elements would break after about 70 runs with substantial warping being visible after about 35. Once we were able to produce better quality material, we could see the quality decline during the last 10-20 runs of the elements life giving the element an even shorter effective lifespan. The coil around the motor shaft has proved even less reliable, and using it has had minimal impact on the material produced. Generally, it has not been used because of the difficulty associated with replacing it and its short lifespan. To fix these issues a new heater setup with a more conventional design and elements made from rhenium is planned for installation in 2014.

CHAPTER 3

Process Development

This chapter describes the development of processes for the deposition of AlN, GaN, and AlGaN on Si(111) substrates using the reactor described in the previous chapter. AlGaN/GaN heterostructures are currently the structures of choice for power devices because of the high mobility and high carrier concentration in the 2DEG that results from the spontaneous and piezoelectric polarization at the interface.[20] Since native bulk substrates for the III-nitrides are prohibitively expensive for most applications, the first step in producing a transistor device is to grow a thick GaN buffer layer on a non-native substrate on top of which the active layers of the device can be deposited.

The most popular substrates for growing III-nitrides are sapphire, SiC, and Si. Sapphire is commonly used for LEDs but substrate sizes are limited and its low thermal conductivity creates heat dissipation issues. SiC has better thermal conductivity but its high cost and small wafer size has limited its use. Si is very attractive as a substrate material because of its low cost and large substrate sizes are readily available. Si also allows for application of the vast body of developed Si processes to be leveraged in production and creates the possibility of integrating III-nitride structures directly with devices made on Si.[37,38] Most electronic devices are fabricated on Si(100) substrates, but the symmetry mismatch between the square surface lattice of the Si(100) and the hexagonal wurtzite structure of the III-nitrides make growing good quality material difficult. The symmetry mismatch issues at the interface can be avoided by using a Si(111) substrate which has threefold symmetry.[37]

Growth of single-crystal (or sometimes referred to as monocrystalline) GaN on Si

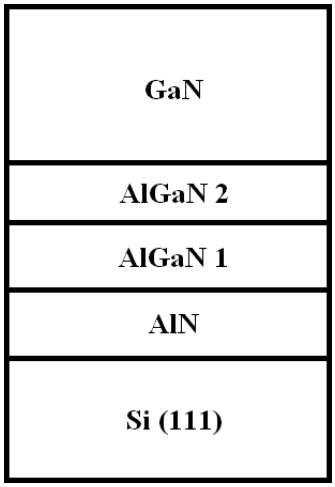

Figure 3.1: Film stack used to deposit GaN on Si.

is challenging because of its tendency to crack when cooling down from deposition due to stress caused by the differences in the coefficients of thermal expansion. To prevent cracking a series of transition layers are used; a typical film stack for the GaN buffer layer is shown in figure 3.1. The coefficient of thermal expansion of AlN more closely matches that of Si, which helps reduce stress during cool down, and its large band gap helps to electrically insulate the device layers from the substrate.

AlGaN layers with decreasing Al content are typically deposited between the AlN layer and the GaN buffer for further stress reduction. The Al content of these layers can either be step-graded[39] or varied continuously.[40] For our purposes we have focused on developing two AlGaN transition layers as shown in figure 3.1 with AlGaN 1 containing 67% Al/33% Ga and AlGaN 2 containing 33% Al/67% Ga. The properties of the individual layers must be tailored to produce a crack-free buffer layer of the desired thickness which can be up to 5 μm depending on the application.[23] The thickness, composition, V/III ratio, and temperature used for growth of these transition layers all must be tuned to produce a buffer layer of the desired thickness.

3.1 Hydrogen Cleaning

The first attempts at depositing AlN at Texas State were made in spring of 2012, and despite the issues with oxygen contamination that were discussed in the previous chapter, progress was made.

When growing on Si, the first step before beginning deposition is to remove the native oxide layer from the substrate. This is done by heating the substrate to the deposition temperature of 1,000-1,100 °C and flowing hydrogen into the chamber to etch the oxide.

In these early AlN depositions the color of the wafer indicated material had been deposited but closer inspection by optical microscope revealed an unexpected surface texture seen in figure 3.2. This texturing was initially believed to be caused by the failure of the AlN to coalesce into a continuous film and consistently appeared throughout the early AlN depositions. The texture is more clearly seen in the SEM image in figure 3.3, and EDS spectra collected from the spots marked in figure 3.3 confirm the presence of AlN. This data supported the hypothesis that the AlN was not coalescing, but when a cross section of this sample was prepared by focused ion beam (FIB) milling and EDS measurements made on the side of one of the raised regions, seen in figure 3.4, the measurements indicated that the raised region was composed only of Si. This suggested that the substrate was damaged prior to deposition and the AlN was only on the surface.

A literature search led to prior work that studied the effects of temperature on the hydrogen cleaning process, and it was found that at below 1,000 °C the etch rate of silicon is higher than that of silicon oxide.[41] Since there are variations in the thickness of the native oxide layer, at lower temperatures some areas of silicon are exposed to hydrogen sooner than others and the remaining oxide acts as a mask resulting in nonuniform etching and the development of pits in the substrate. From this data it was suspected that the slow heat up under hydrogen, performed as a

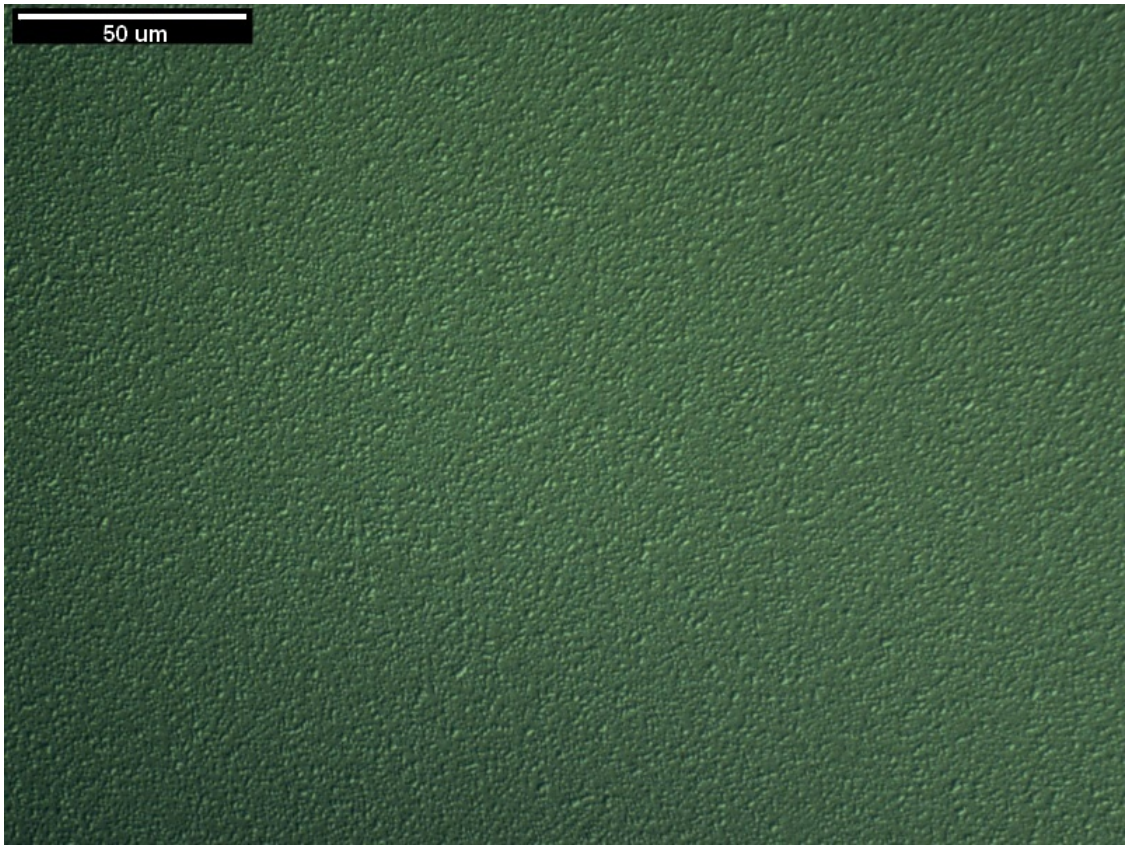

Figure 3.2: 50x Nomarski image showing surface texturing.

precaution against breaking the substrate due to nonuniform thermal stress, was causing the pitting.

In order to test this, Si wafers were heated under various conditions and then cooled under nitrogen without deposition. Figure 3.5a is an AFM image of a wafer that was heated under hydrogen using the slow temperature ramp that was suspected of causing the pitting seen in the AlN runs, and confirms there was significant damage to the substrate even before AlN deposition began. In figure 3.5b the sample was heated under hydrogen at the maximum rate possible, which at the time was limited by the output of the heater power supply. The morphology indicates improvement compared to the sample seen in figure 3.5a, but still has significant pitting. To avoid the low temperature etching, the heat up procedure was modified so that the substrate is initially heated under nitrogen which is

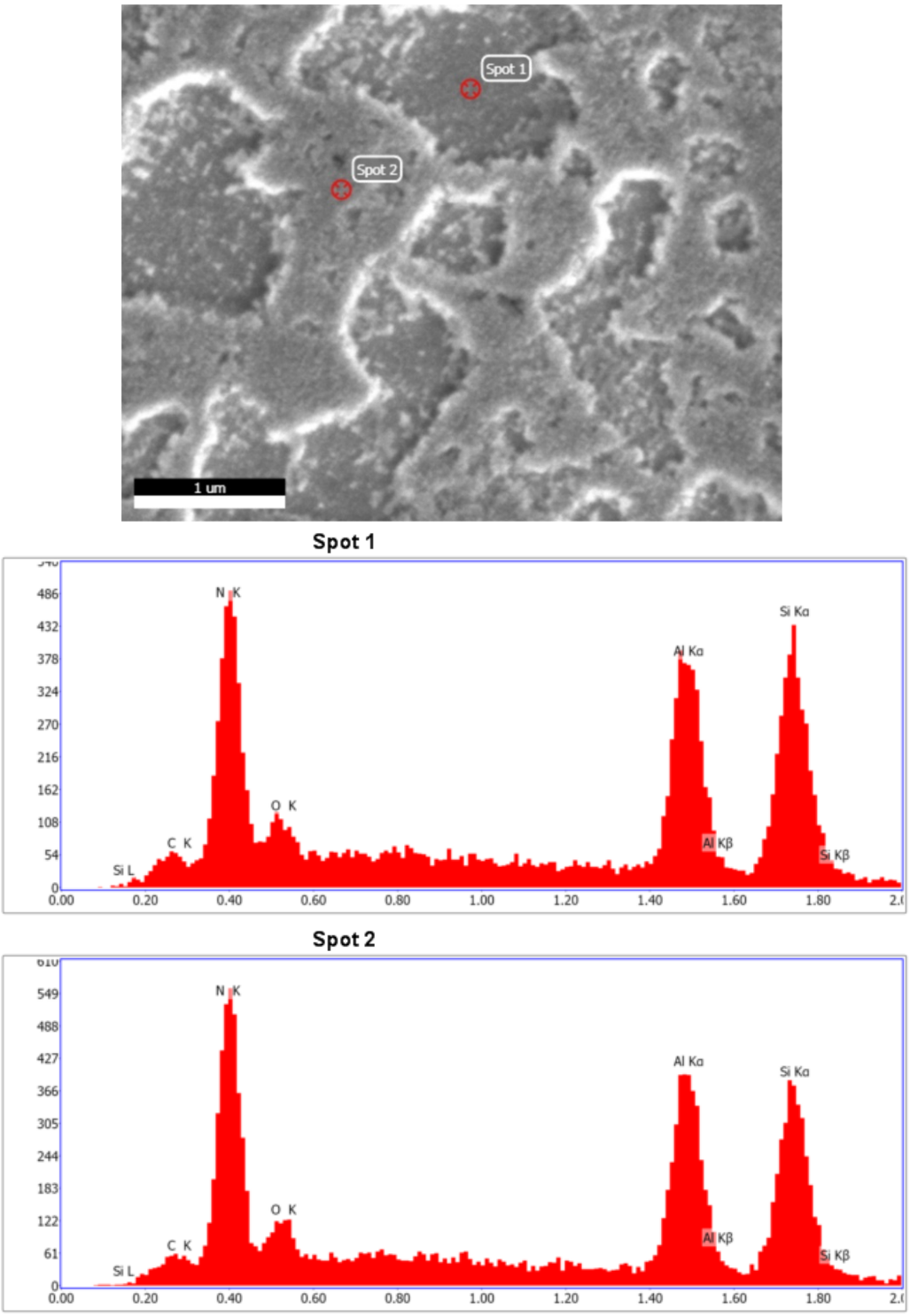

Figure 3.3: SEM surface and EDS scans on pits.

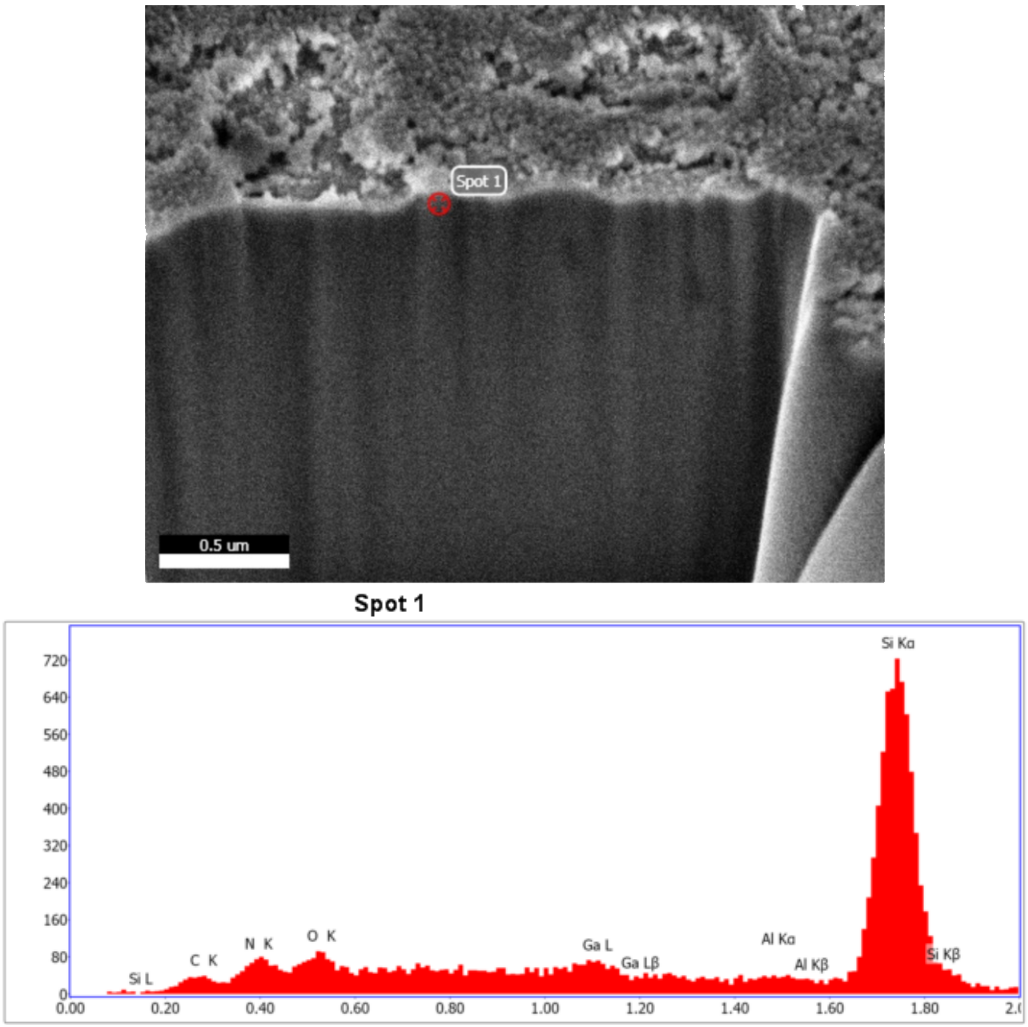

Figure 3.4: Cross section of AlN with pitting.

replaced with hydrogen once the temperature has reached 1,000 °C. After the hydrogen is switched on, the temperature is increased to the deposition temperature where it is allowed to stabilize. The results of this procedure are shown in figure 3.5c, and the morphology of the surface indicates no damage to the substrate.

3.2 AlN

Once the heat up issues were identified and resolved the first successful AlN deposition without pitting was achieved immediately thereafter. Continuing incidents of oxygen contamination hindered further process development until early

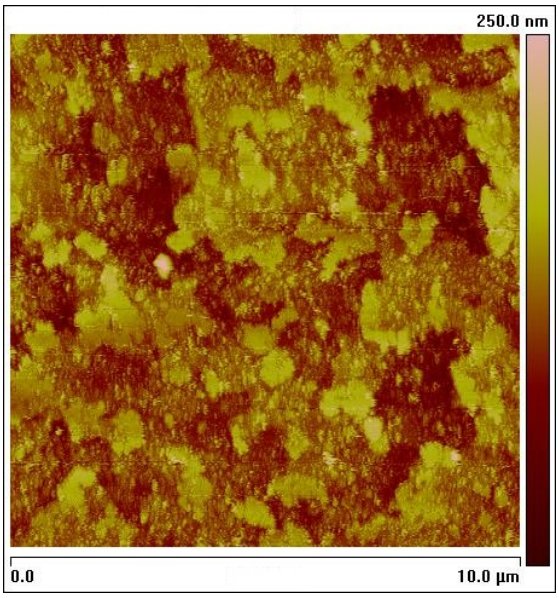

(a) Slow heat up under H_2

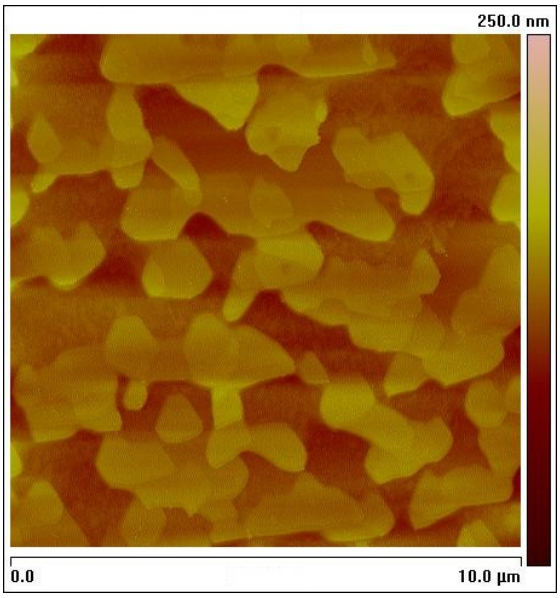

(b) Rapid heat up under H_2

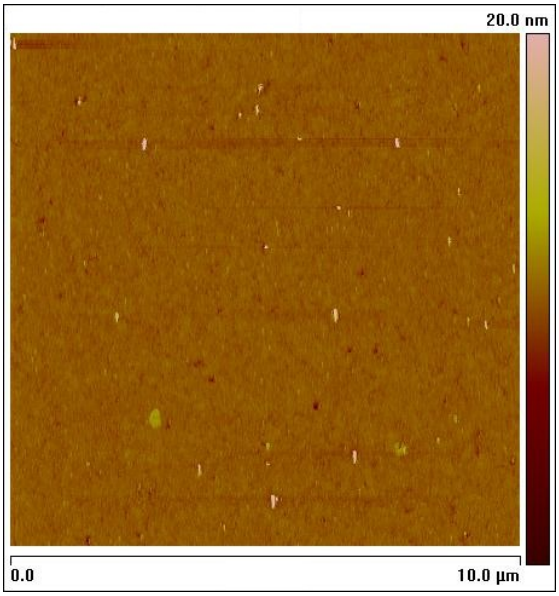

(c) Heat up under N_2

Figure 3.5: AFM images of the Si substrate surface after heating.

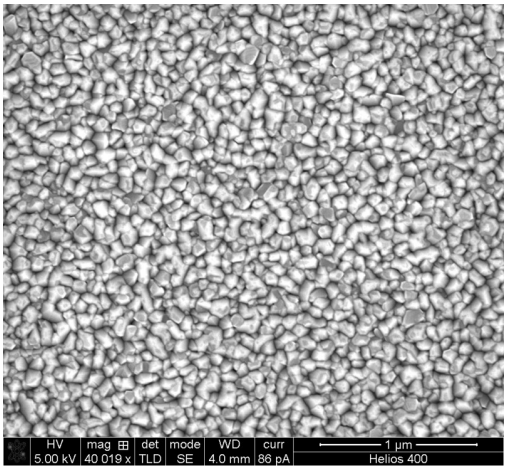

(a) 1550 °C, V/III 1200

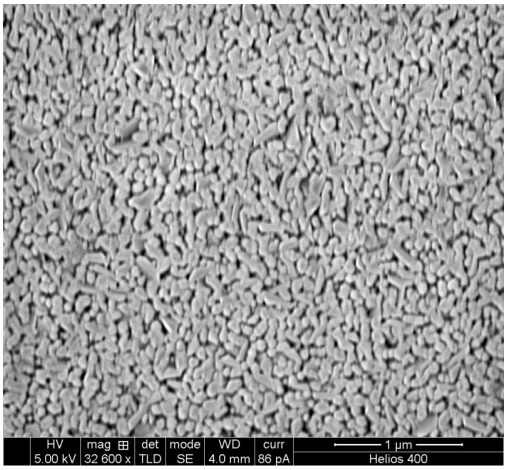

(b) 1425 °C, V/III 1200

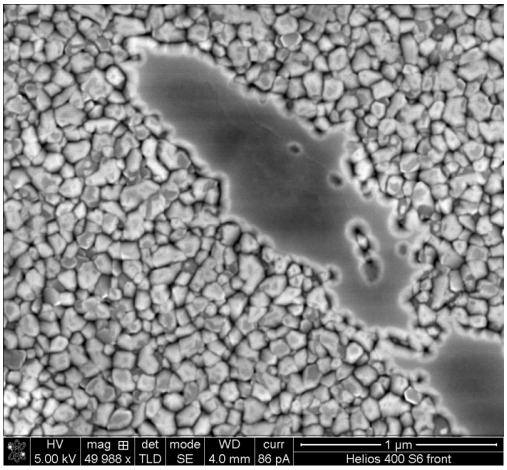

(c) 1550 °C, V/III 900

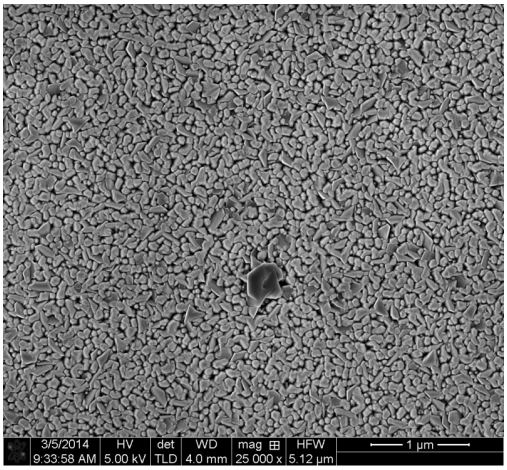

(d) 1425 °C, V/III 900

Figure 3.6: AlN variation with heater temperature and V/III ratio.

2013 when those issues were finally addressed. With the reactor finally stable, a series of samples was made varying the V/III ratio and the heater temperature. The SEM images shown in figure 3.6 show representative examples from this study.

AlN is typically grown at a V/III ratio of $\sim 1,000$ or less and a temperature of 1,100 °C.[42] It should be noted that the temperatures listed in figure 3.6 are the temperatures measured by the heater thermocouple and not the substrate temperature. The thermocouple reading is approximately 500 °C higher than the surface temperature as measured by the pyrometer. This difference can vary significantly based on the condition of the thermocouple and the coating of the

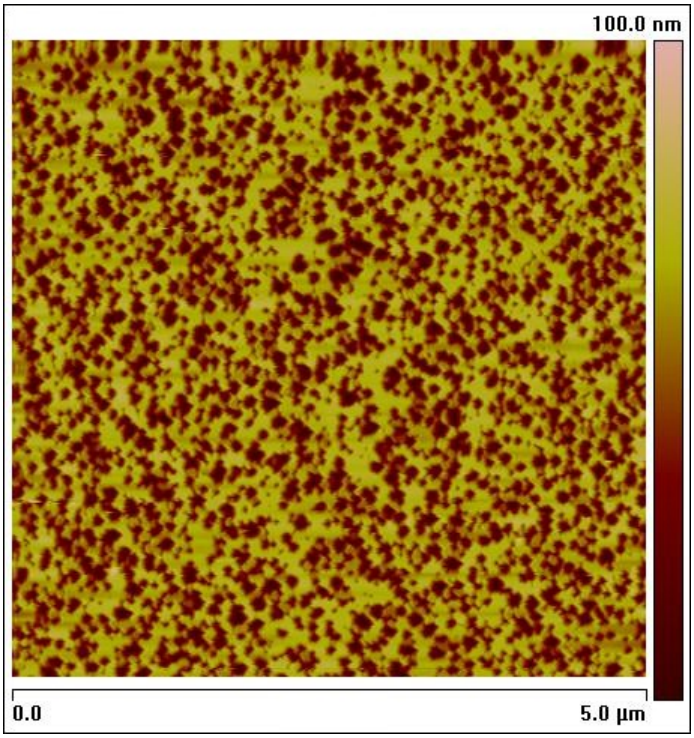

Figure 3.7: AFM image of AlN grown at higher temperature.

chamber walls. The samples grown at 1425 °C seem to have flatter tops and more elongated grains compared to the pebbled, more crystallographically oriented surface seen in the samples grown at 1550 °C. There appears to be minimal change with the V/III ratio in the samples grown at 1425 °C, however in the sample grown at 1550 °C and a V/III ratio of 900, shown in figure 3.6c, regions where the grains had coalesced could be seen.

There is no clear relationship between the properties of the AlN layer and the quality of the layers that can be grown on top of it. Ultimately it has been necessary to go to even higher temperatures to grow good quality GaN. With further process optimization, deposition of AlN is conducted with the heater temperature set to ∼1650 °C and a V/III ratio of 980. An AFM image of the more recent AlN films is shown in figure 3.7. Using the heater thermocouple to set the deposition temperature has proven to be unreliable because the reading drifts as the heater element ages and warps over the course of several runs. The solution to this

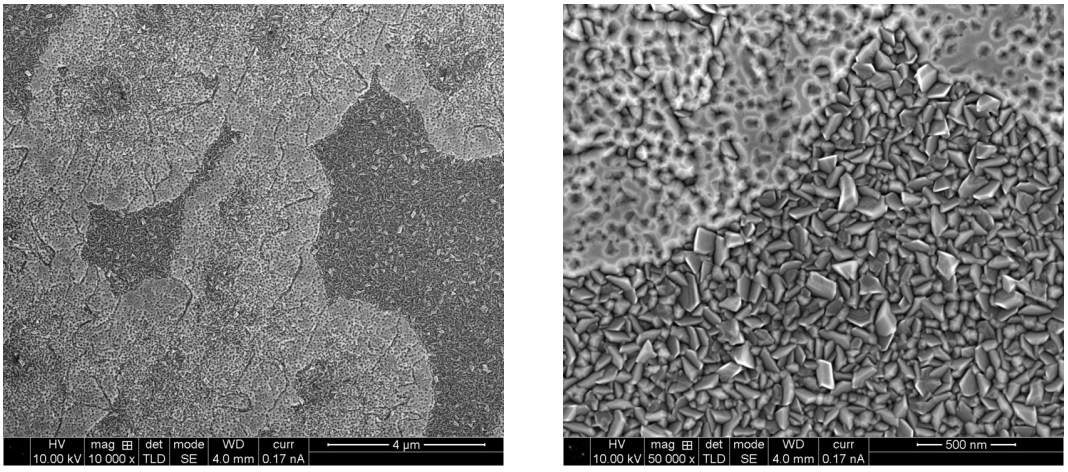

(a) (b)

Figure 3.8: AlN grown shortly before a heater element failed.

has been to adjust the heater temperature as needed to reach the desired temperature as measured by the pyrometer.

The simplicity of a single AlN layer makes it useful for monitoring the uniformity of the deposited material, which will be discussed later, and for diagnosing issues with the reactor. For example, in figure 3.8 an AlN sample was grown shortly before a heater element failed and shows a mixture of coalesced, single-crystal regions and polycrystalline regions. The lighter regions in figure 3.8a and in the upper left of figure 3.8b show where the AlN has coalesced.

3.3 GaN

After the reactor had proved stable over the course of several AlN depositions, work began on depositing a GaN layer on the AlN. The early GaN depositions were conducted at lower temperatures because of the power supply limitations, and had a matte grey appearance with almost no reflectivity caused by the roughness of the film. This roughness can be seen in figure 3.9 which shows a back scattered electron SEM image of GaN on AlN. The lighter contrast, raised features are GaN crystals and the darker areas indicate regions of AlN are not covered by GaN. From these

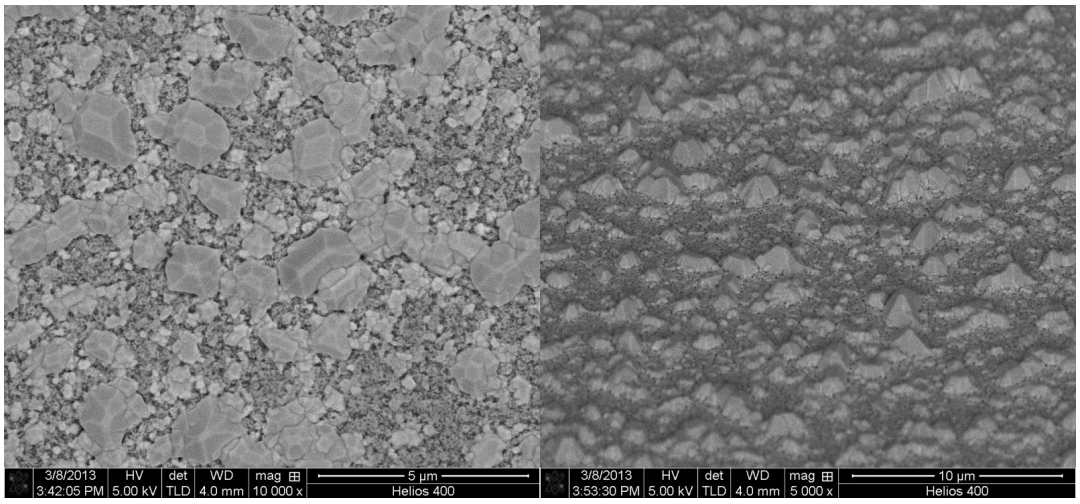

Figure 3.9: GaN on AlN prior to power supply replacement.

images it is clear that the GaN layer is not coalescing to form a single-crystal layer, similar to what was originally believed to be occurring with the AlN. Increasing the TMG flow improved the coverage of the AlN but the islands still did not coalesce. At this point it was suspected that the deposition temperature was too low, and a new power supply was installed to rectify this issue.

After replacing the power supply, there was a substantial improvement of the quality in the GaN. Growing both the AlN and GaN at higher temperatures caused the GaN to coalesce completely covering the AlN and adjustments to the V/III ratio significantly improved the surface roughness of the GaN film as can be seen in figure 3.10a. This sample was grown prior to installing a new chiller for the reactor diffuser plate and is noticeably rougher than the sample shown in figure 3.10b, which was grown under similar conditions with the new chiller. With the old chiller setup, the temperature of the diffuser plate was not adequately controlled and increased over the course of a run which likely led to reactions of the precursors before they reached the substrate causing the roughness. The sample shown in figure 3.10b was confirmed to be single-crystal material by HRXRD measurements shown in figure 3.11 and the rocking curve of the GaN peak was measured to have a full width at half-maximum (FWHM) of 832 arcsec. This compares well to the FWHM value of

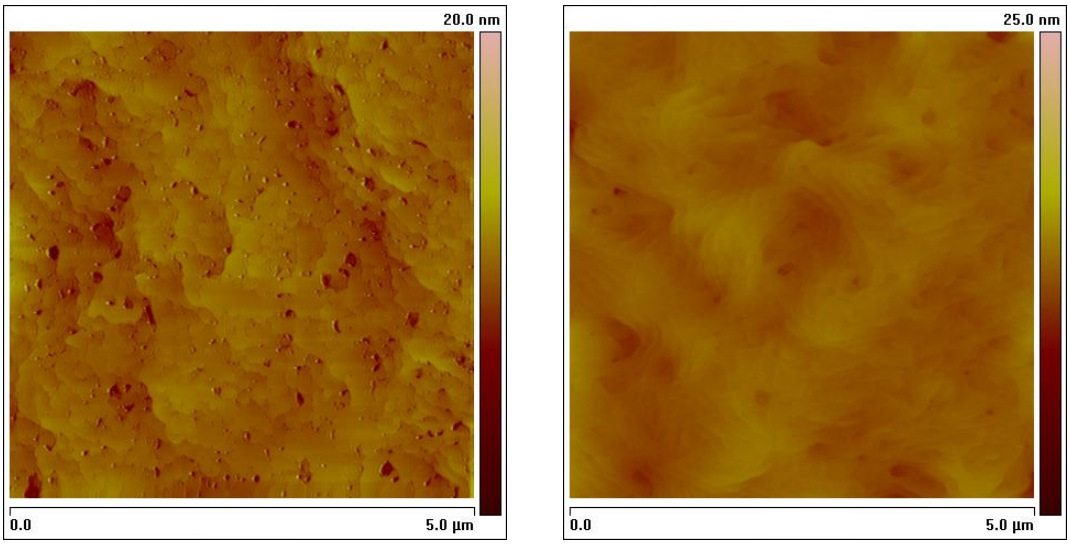

(a) Prior to chiller replacement (b) After chiller replacement

Figure 3.10: Effect of diffuser plate chiller on GaN surface.

656 arcsec that has been reported for growth of GaN on an optimized AlN layer.[43] A cross section of the same sample prepared by FIB, shown in figure 3.12, shows a growth rate of 0.75 μm/hr for the AlN and 1.5 μm/hr for the GaN.

A new pyrometer was installed along with the power supply and has proved extremely useful as a process monitoring tool. The pyrometer that was donated with the system is an older model that only displays the current temperature reading, whereas the new unit has software to display a real time graph of the temperature and can log the data. Figure 3.13 shows temperature data collected during deposition for a single 50 mm wafer and a 150 mm wafer with the same growth conditions. The temperature data collected from the 150 mm wafer shows well defined oscillations that are the result of optical interference between the reflections from the substrate and the film as it grows. The larger, lower frequency oscillation at the beginning of the deposition is from the growth of the AlN layer and the smaller, higher frequency oscillations that begin near the 40 minute mark are from the GaN layer. The difference in the frequency of the oscillations of the AlN and the GaN is due to the higher growth rate of the GaN compared to the

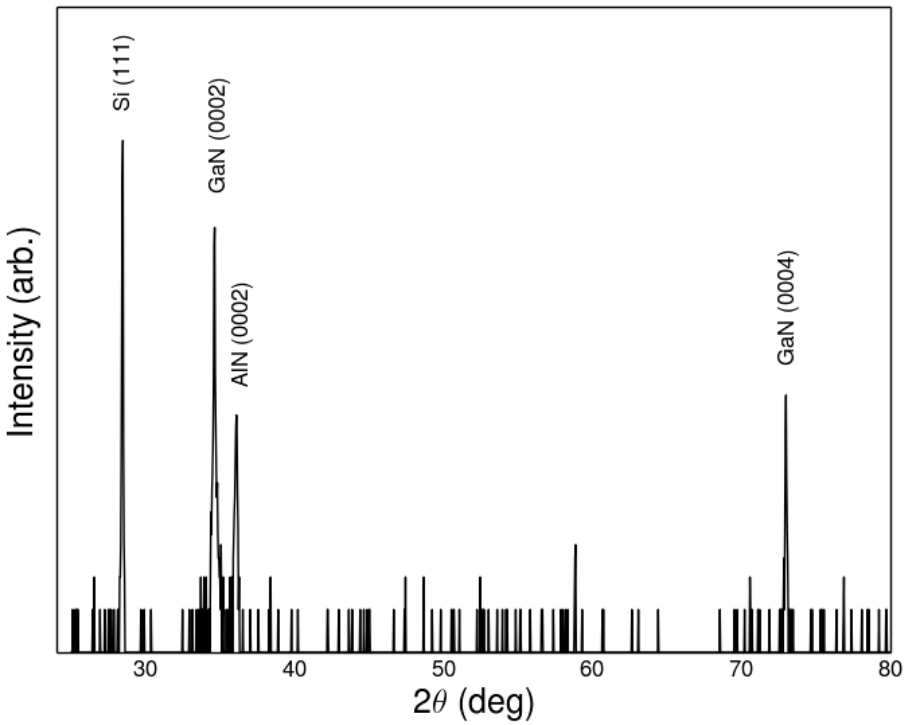

Figure 3.11: Confirmation of single-crystal GaN by HRXRD.

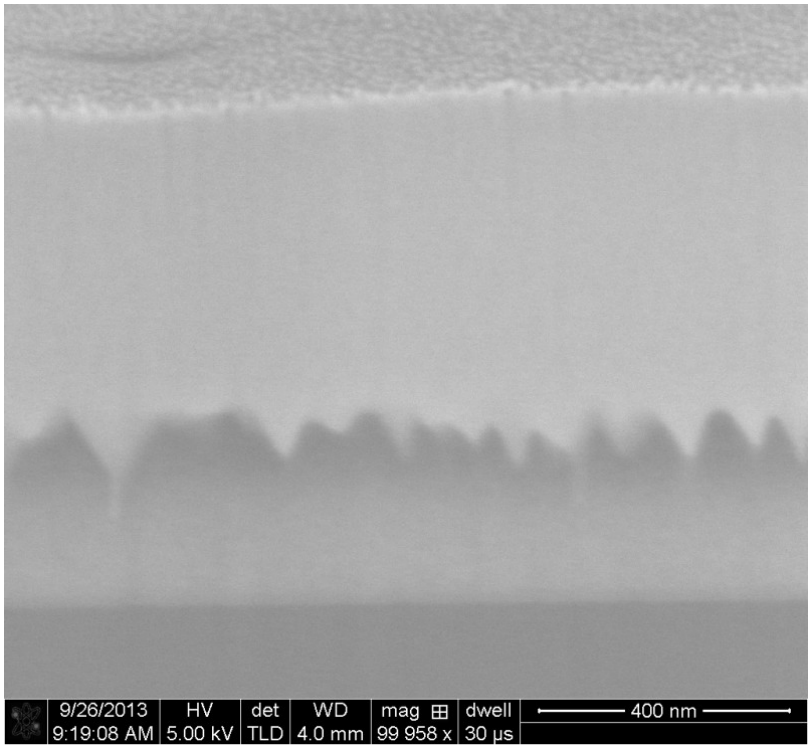

Figure 3.12: Cross sectional SEM image showing GaN and AlN layers.

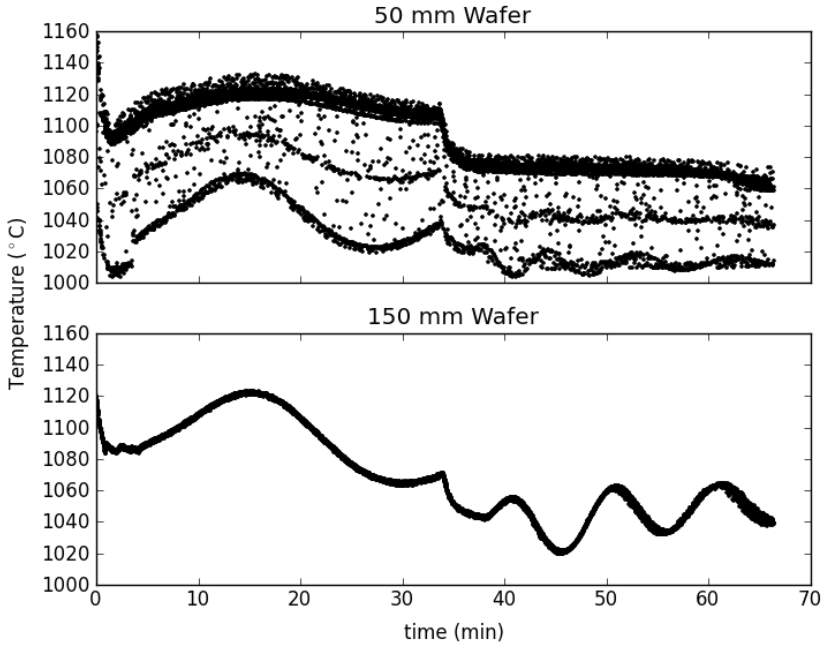

Figure 3.13: Pyrometer data for 50 mm and 150 mm wafers.

AlN. Experience has shown that these oscillations consistently appear for the AlN layer, but will quickly decay to a constant value if poor quality GaN is being grown.

The data collected from the 50 mm wafer is more difficult to interpret because the pyrometer is collecting data from both the substrate and the susceptor, and often a combination of the two. Three distinct temperature readings can be seen in the 50 mm wafer data: the broad top line, a strong bottom line that generally follows the oscillation pattern of the 150 mm wafer, and a weaker line in the middle that also follows the oscillation pattern. The top line is most likely readings from the susceptor, however there is not a clear interpretation of the other two lines. The data from the 150 mm wafer most nearly corresponds with the middle line and it is reasonable that the fewest measurements would come directly from the wafer, hence why it has the fewest data points. However, if the bottom line is from a combination of the wafer and susceptor it should be higher than the temperature of the wafer because of the higher reading from the susceptor.

3.4 AlGaN and Uniformity

Following the demonstration of good quality GaN could be produced research was undertaken to develop the $Al_xGa_{1-x}N$ transition layers with $x = 0.67$ and $x = 0.33$. Throughout the development of the AlN and GaN processes the coloration of the deposited films indicated variations in the thickness caused by the flow dynamics in the chamber. It is not surprising that this would lead to variation in the composition of the AlGaN layers across the wafer as well.

Figure 3.14 shows the composition of two AlGaN films, determined from HRXRD measurements using Vegard's law, as a function of the radial distance from the center of a 150 mm wafer. The composition is assumed to be azimuthally uniform because of the substrate rotation during deposition. Generally the peaks are too weak at distances less than 25 mm or greater than 65 mm to determine the composition. This is attributed to a cool spot near the center due to the motor shaft and insufficient heating near the edge due to the heater design. In the sample shown, the peaks were sufficiently intense that the composition can be determined across the entire 150 mm. Both AlGaN layers follow the same general trend and show a maximum variation of about 10% across the region between 25 and 65 mm.

In addition to the uniformity issues, the problems with the flow dynamics in the reactor also led to particles being deposited on the wafer during deposition. The presence of particles on the wafer after deposition had been noticed, but the addition of the AlGaN layers to the film stack increased the deposition time and the issues with the particles became more pronounced. The images shown in figures 3.15 and 3.16 indicate the particle coverage is fairly dense in the region halfway between the wafer center and edge. There are significantly fewer particles in the center and closer to the edge of the wafer. From these images it can be seen that the particles form two types of structures; either a particle can become covered during deposition creating raised regions that appear as the colored speckling in

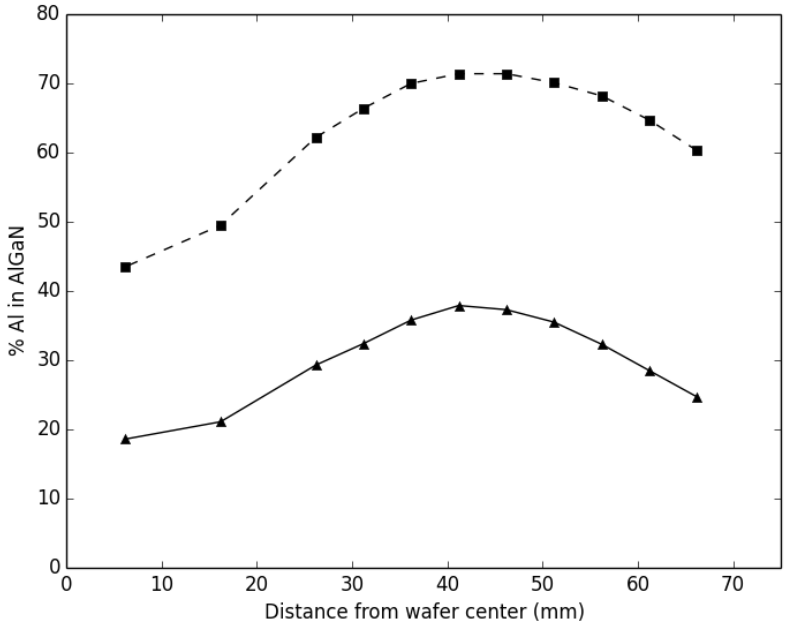

Figure 3.14: Compositional variations of the two AlGaN layers across a 150 mm wafer.

3.15, or it can form a hollow dome structure as seen in figure 3.17 which are the larger black circles in figure 3.15.

The severity of the particle coverage means this issue must be addressed before further process development progress can be made. The particles are a result of recirculating flows in the reactor chamber, and if the proper flow conditions are found, not only should there be a reduction in particles but the films will have a more uniform thickness across the wafer and the compositional variation of the AlGaN layers will be reduced. Since all three of these issues are linked, the simplest approach to fixing them is to start by improving the thickness uniformity of the AlN.

It was found that there were relatively fewer particles when the inner, middle and outer alkyl injectors were set to 1,500 sccm, 1,000 sccm, and 5,500 sccm respectively and the hydride injectors set to twice those rates. These are the same flow conditions used in the the deposition of the AlGaN layers seen in figure 3.14. Using these settings as a control, a series of AlN samples was made varying each

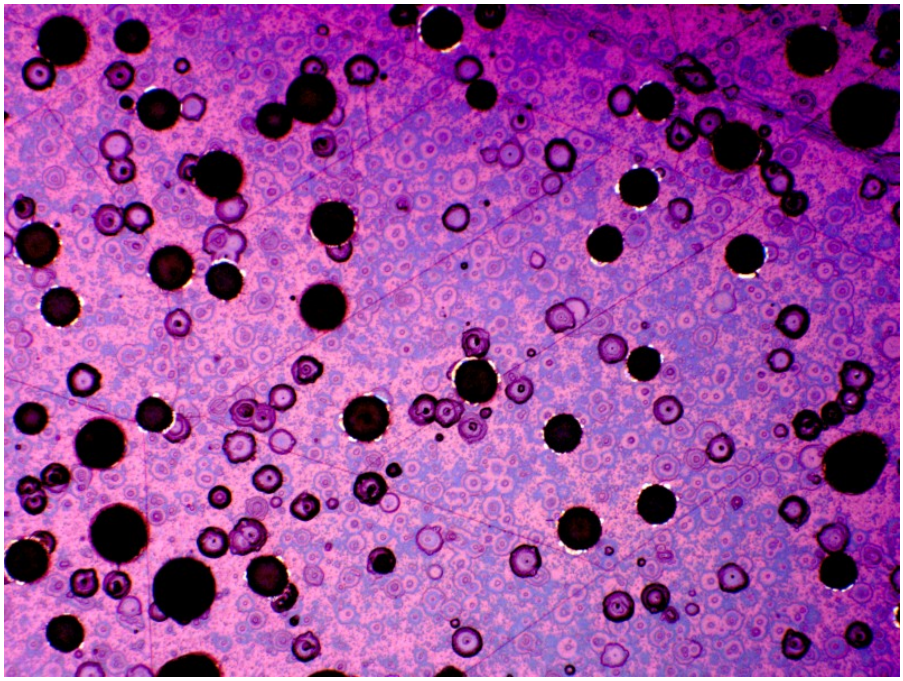

Figure 3.15: 20x optical microscope.

injector's flow individually by ±500 sccm. The results of decreasing the flows are seen in figure 3.18 and increasing them in figure 3.19.

The variations in thickness indicate that the flow changes are having an impact on the flow dynamics but the overall thickness profile remains the same. It is reasonable to expect that the thickest part of the film would shift as the flows are varied. Since this does not occur it suggests there is some other factor that is causing the problem such as the rotation rate of the substrate or the temperature non-uniformity from the heater. The thickest part of the AlN matches closely with the position of the highest Al concentration in the AlGaN film in figure 3.14, which supports the idea that if the uniformity of the AlN thickness is improved there will also be an improvement in the compositional uniformity of the AlGaN layers.

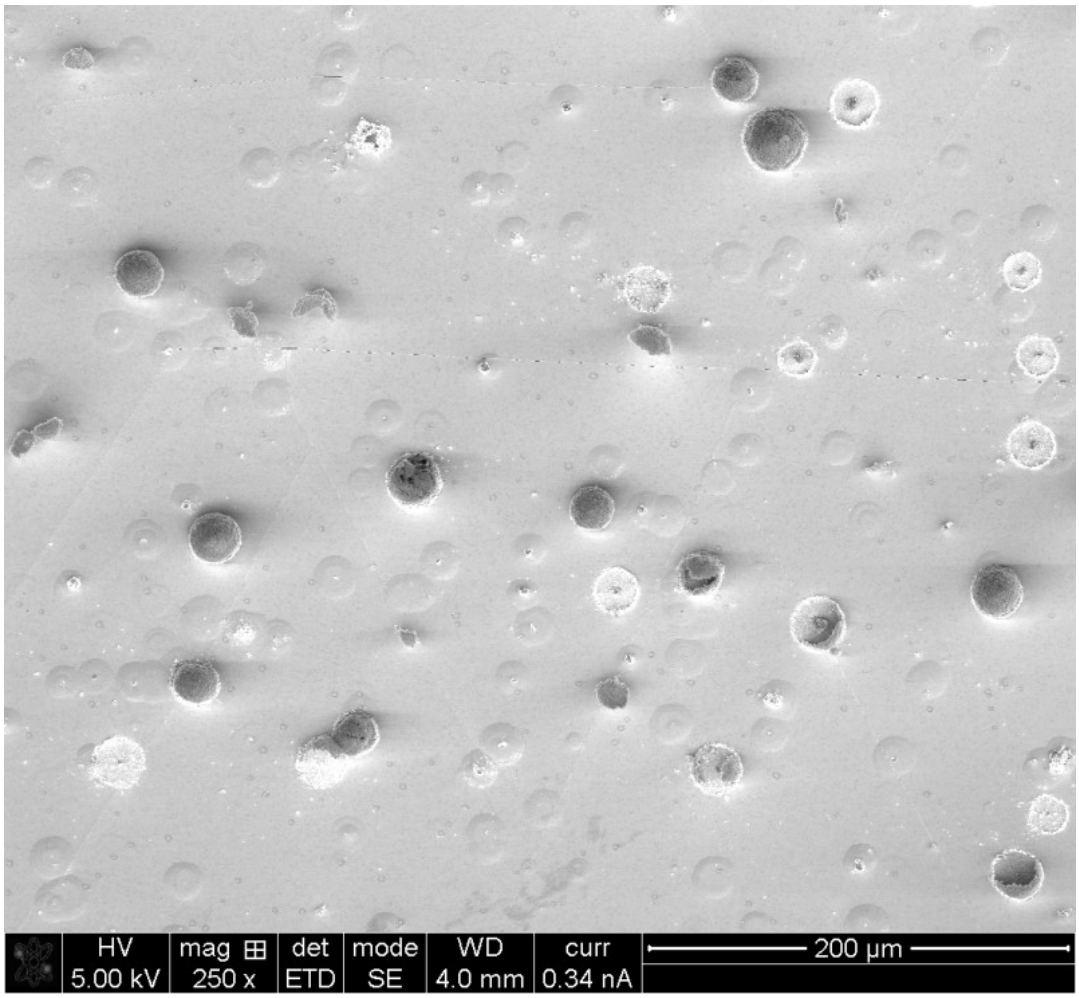

Figure 3.16: 250x SEM image.

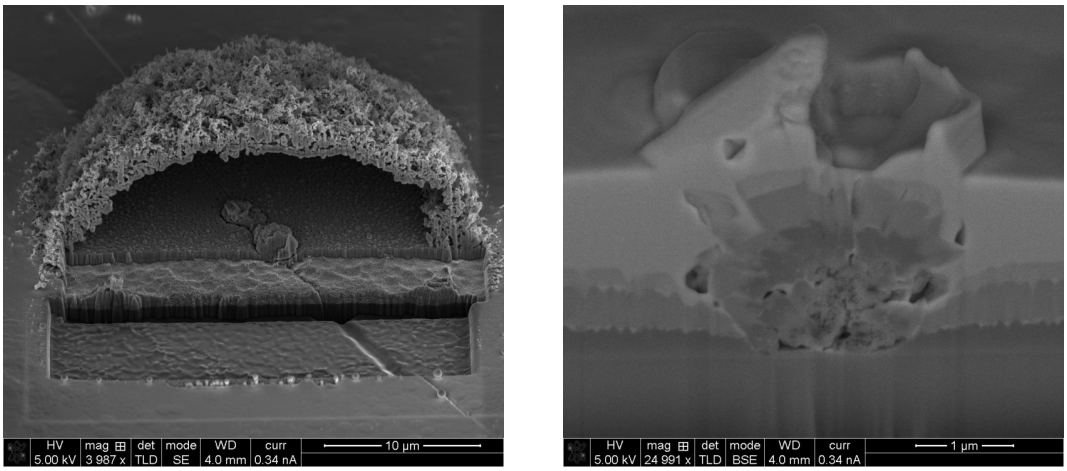

Figure 3.17: SEM cross sections of particles.

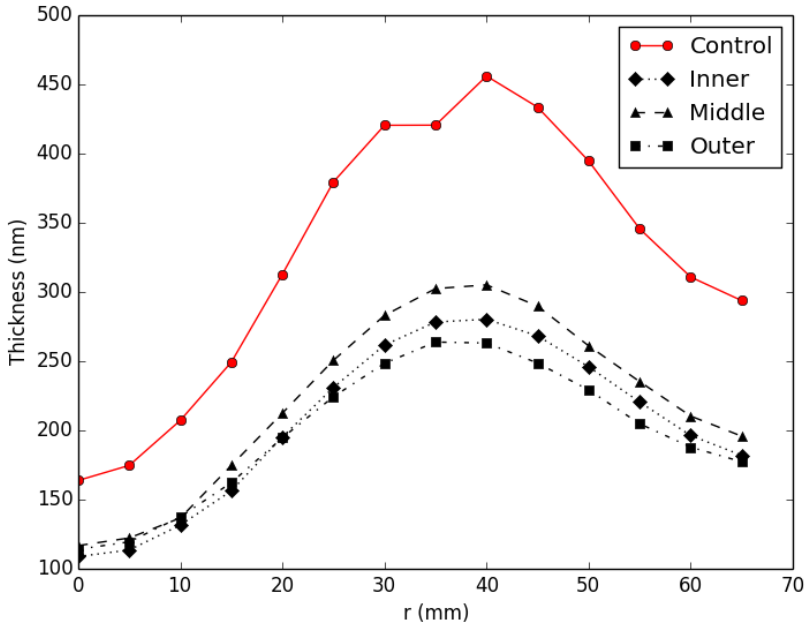

Figure 3.18: Effect of decreasing injector flows 500 sccm on thickness.

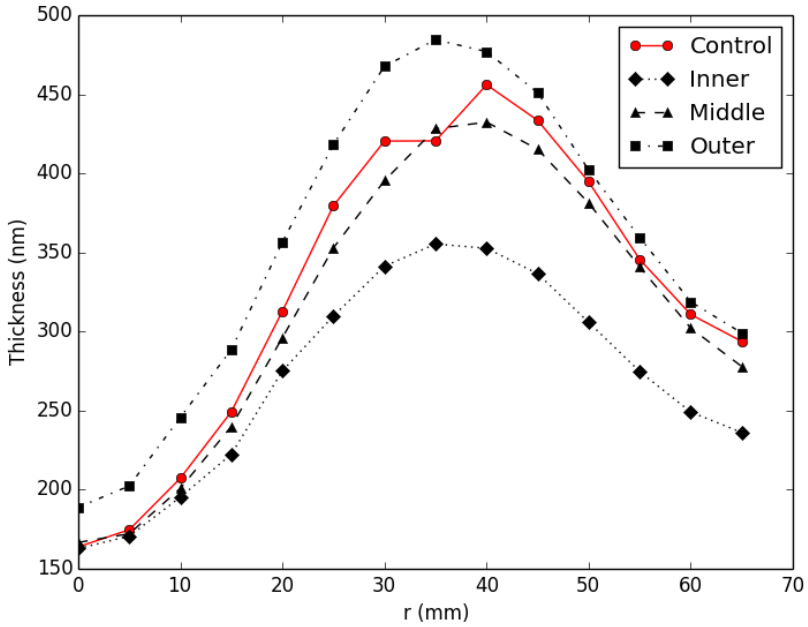

Figure 3.19: Effect of increasing injector flows 500 sccm on thickness.

CHAPTER 4

Investigation of AlGaInN Microstructure

This chapter presents a study of AlGaInN by scanning transmission electron microscopy (STEM). The principle purpose of the study was to determine if clusters of In are forming within the film as has been predicted.[18,28] The thermodynamics of phase separation in the context of the regular solution model will be presented, as well as the theoretical predictions for the quaternary sample studied. The basic principles of STEM will also be discussed with an emphasis on high-angle annular dark field imaging. Finally, the results of the analysis of a 10 nm thick AlGaInN film grown at 750 °C containing 3-6% Ga and 14-17% In that was provided by IQE will be discussed, and conclusions drawn.

4.1 The Regular Solution Model

The regular solution model describes the thermodynamics of mixing of the components of a solution and gives insight into the physics of compositional phase separation. Previous studies have shown it to be reasonably accurate for the ternary III-nitrides.[36] The theory behind the model will be presented for the case of a two component solution, which can be used to model ternary $A_xB_{1-x}C$ compounds, and the results of extending it to three components, required to apply it to AlGaInN, will then be discussed. The goal of the regular solution model is to allow the calculation of the Gibbs molar free energy, ΔG which can be written in terms of the enthalpy H, entropy S, and absolute temperature T as

$$\Delta G = \Delta H - TS. \tag{4.1}$$

In the regular solution model with two components the entropy is calculated by assuming there are N_A atoms of type A and N_B atoms of type B. The A and B

atoms are distributed among $N = N_A + N_B$ lattice sites. The number of ways these two types of atoms can be distributed is given by

$$\frac{N_A!}{N_A!N_B!}, \tag{4.2}$$

and by using Stirling's approximation the molar entropy can be calculated from equation 4.2 to be[44]

$$S = -R\left(x \ln x + (1-x)\ln(1-x)\right) \tag{4.3}$$

where R is the molar gas constant and x the mole fraction of component A.

In general the enthalpy can be written as

$$\Delta H = \Delta E + P\Delta V. \tag{4.4}$$

In the regular solution model it is assumed that $\Delta V = 0$, that is there is no change volume when the components mix. This reduces equation 4.4 to $\Delta H = \Delta E$ which shows the free energy is independent of pressure as well as volume. The enthalpy is assumed to have the form

$$\Delta H = \Omega x(1-x). \tag{4.5}$$

The constant Ω accounts for the interactions between the mixing species, and can be written in terms of the number of bonds per atom z, the number of atoms N, the bond energies between atoms of the same type E_{AA} and E_{BB}, and the bond energies between atoms of different types E_{AB}, as[44]

$$\Omega = zN\left(E_{AB} - \frac{1}{2}\left(E_{AA} + E_{BB}\right)\right). \tag{4.6}$$

With these expressions for the enthalpy and entropy equation 4.1 can be written as[44]

$$\Delta G = \Omega x(1-x) + RT\left(x \ln x + (1-x)\ln(1-x)\right). \tag{4.7}$$

If $\Omega > 0$ the enthalpy term is positive and the entropy term is negative in equation 4.7, and it is possible to define the critical temperature as $\Omega/2R$. If the

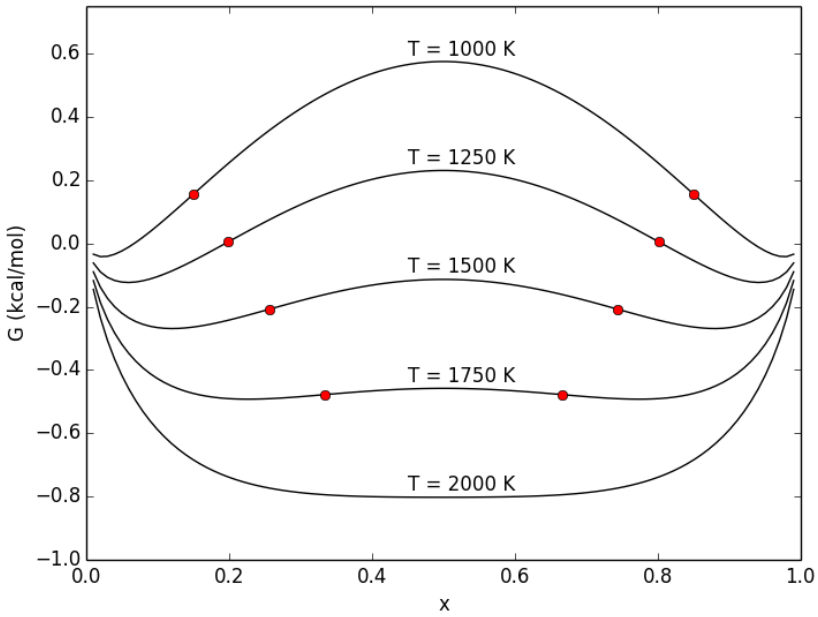

Figure 4.1: Variation of free energy with temperature.

temperature is above the critical temperature, the entropy term will dominate making the free energy negative for all compositions. However if the temperature is below the critical temperature, a region with negative curvature can develop creating a miscibility gap as shown in figure 4.1. The compositions at which the free energy is a minimum and the compositions of the inflection points, which satisfy

$$\frac{\mathrm{d}^2\Delta \mathrm{G}}{\mathrm{d}x^2} = 0, \tag{4.8}$$

are used to plot the binodal and spinodal curves respectively to create the phase diagram. In figure 4.1 the inflection points are marked with red dots, and the compositions at which they occur can be seen to vary with temperature.

Each free energy curve below the critical temperature has two inflection points at compositions s_1 and s_2, which vary based on the temperature. The spinodal curve is then generated by plotting the pairs (s_1, T) and (s_2, T) as is illustrated in figure 4.2. Similarly, the binodal curve is generated by finding the compositions for which the free energy is minimized, X_1 and X_2 in the example and shown in figure

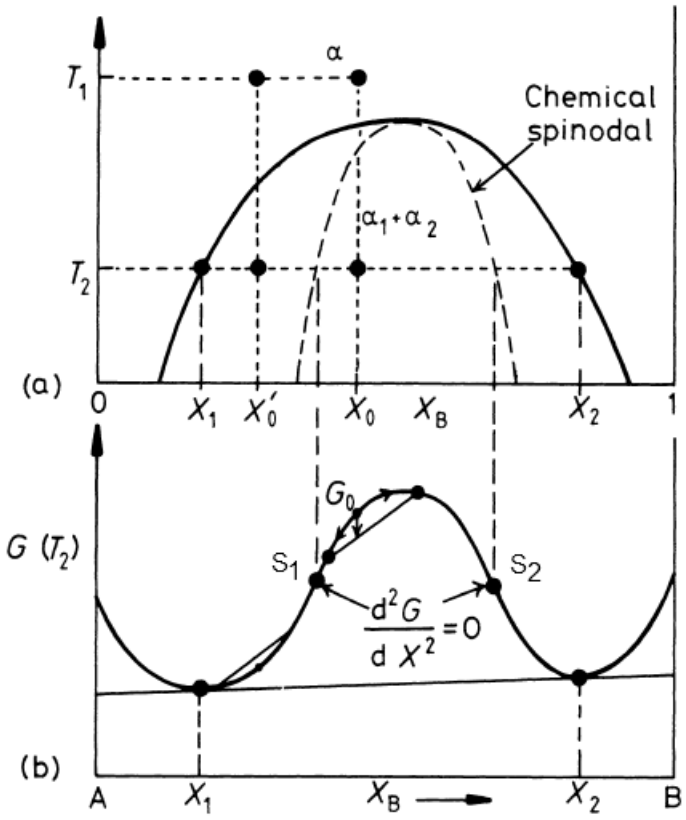

Figure 4.2: Illustration of phase diagram construction.[45]

4.2, for a given temperature and then plotting the points (X_1, T) and (X_2, T).

The spinodal and binodal curves divide the plane into three regions seen in figure 4.2. Within the area area bounded by the spinodal curve the alloy is unstable and small fluctuations in composition cause the spontaneous formation of clusters of atoms. Between the binodal and spinodal curves the alloy is metastable and additional energy is required to change the composition. Outside of the binodal curve the components of the alloy are completely miscible.[45]

The regular solution model can be extended to systems where the mixing of three components occurs, and the free energy of mixing for a quaternary alloy of the type $A_{1-x-y}B_xC_yD$ can be shown to be[18]

$$\begin{aligned}\Delta G = &\Omega_{BC}xy + \Omega_{AB}x(1-x-y) + \Omega_{AC}y(1-x-y) + \\ &RT\left(x\ln x + y\ln y + (1-x-y)\ln(1-x-y)\right).\end{aligned} \tag{4.9}$$

In equation 4.9 the Ω terms again represent the interactions between the different atomic species and are taken to be the same as the parameters used in equation 4.7. Equation 4.9 has the same general form as the free energy for a two component solution where there are terms to account for the interaction between each of the different atoms and an entropy term. It can also be seen to reduce to equation 4.7 if either x or y is zero.

In analogy to equation 4.8 the inflection points for a function of two variables must satisfy

$$\left(\frac{\partial^2 \Delta G}{\partial x^2}\right)\left(\frac{\partial^2 \Delta G}{\partial y^2}\right) = \left(\frac{\partial^2 \Delta G}{\partial x \partial y}\right)^2. \tag{4.10}$$

This expression is used to find the points needed to generate the spinodal curve for a three component solution.[18] For the free energy given in equation 4.9 this yields

$$(RT)^2 = RT\left[2\Omega_{BC}xy + 2\Omega_{AB}x(1-x-y) + 2\Omega_{AC}y(1-x-y)\right] + F_\Omega xy(1-x-y) \tag{4.11}$$

where

$$F_\Omega = \Omega_{AB}^2 + \Omega_{AC}^2 + \Omega_{BC}^2 - 2(\Omega_{AB}\Omega_{AC} + \Omega_{AB}\Omega_{BC} + \Omega_{AC}\Omega_{BC}) \tag{4.12}$$

As can be seen from equation 4.11, the spinodal curve for a solution with three components is determined by three variables: the temperature and two of the compositions. In order to visualize the results of equation 4.11 for the sample in this study, graphs were generated by fixing one of the variables and plotting the remaining two.

As written the equation 4.11 is quadratic in T, and can be used to generate a phase diagram similar to the one seen in figure 4.2a. This was done by solving the quadratic equation for 4.11 to find T, and plotting the result assuming a Ga content of 4%, that is $x = 0.04$ and allowing the In content y to vary in the range $0 < y < 0.96$. This shown in figure 4.3 and the points marked in red represent the upper and lower estimates of the In content at 750 °C. Alternatively, equation 4.11

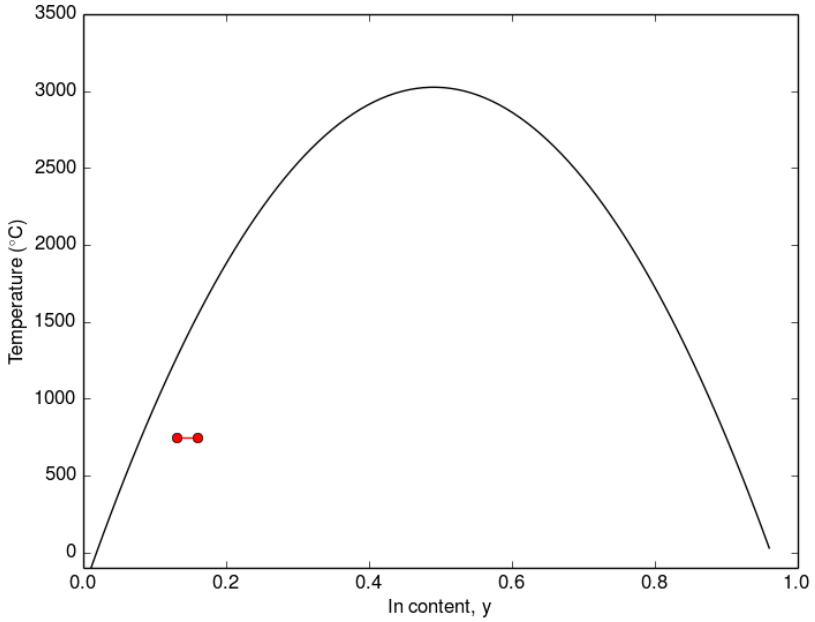

Figure 4.3: Pseudo-binary spinodal curve for AlGaInN with 4% Ga.

can be rearranged as a quadratic in y as

$$\begin{aligned}&(F_\Omega x + 2RT\Omega_{AC})y^2 \\ &- [F_\Omega x(1-x) + 2RT(x(\Omega_{BC} - \Omega_{AB} - \Omega_{AC}) + \Omega_{AC})]y \\ &- 2RT\Omega_{AB}x(1-x) + (RT)^2 = 0\end{aligned} \tag{4.13}$$

Again, the value of y can be calculated using the quadratic equation as a function of x and T. For fixed T, this gives the three compositions x, y, and $1-x-y$, which can then be plotted using a ternary diagram shown in figure 4.4. The estimated range of compositions is marked in red, and the black line shows the spinodal isotherm calculated for 750 °C.

From figures 4.3 and 4.4 it is seen that the composition of the sample studied lies within the spinode, so it is expected that phase separation as a result of spinodal decomposition will occur. In addition to these predictions using the regular solution model, more sophisticated modeling has been done using *ab initio* total energy electronic structure calculations combined with Monte Carlo simulations also

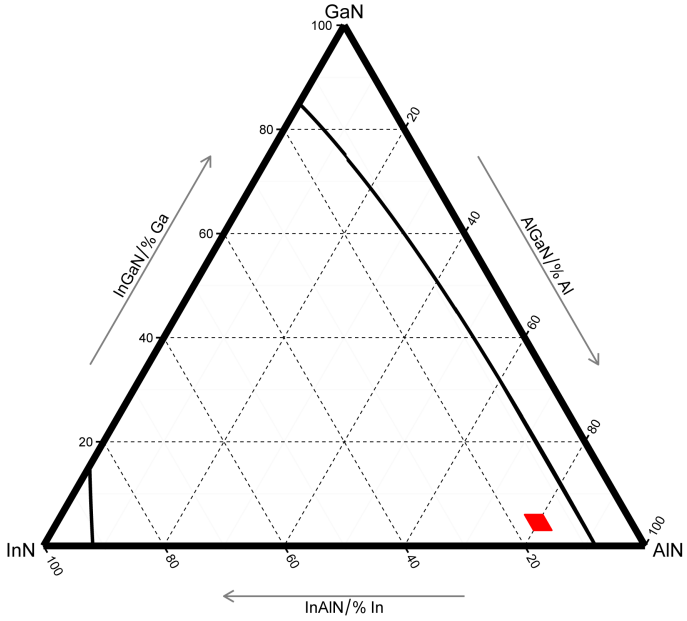

Figure 4.4: Spinodal isotherm calculated for 750 °C.

predict that phase separation should occur for this sample, and in particular only In shows a tendency to form clusters.[28]

4.2 Scanning Transmission Electron Microscopy

Several methods have been used to observe phase separation in materials including: x-ray diffraction, Raman scattering, photoluminescence, and transmission electron microscopy (TEM).[29] With the exception of TEM, there are limitations to the resolution with which the sample can be probed using these techniques. If there are composition fluctuations occurring on a scale below the resolution of the instrument, they will be detected but the detailed information of the microstructure becomes difficult or impossible to discern.

In microstructural investigations by conventional TEM (CTEM) evidence of phase separation by spinodal decomposition is often observed as a tweed pattern in the image, as well as in fine structure in the selected area diffraction pattern.

However, it is difficult to extract structural information from CTEM images because of the coherent nature of the technique. These coherence effects cause contrast variations based on the sample thickness and the focus conditions used. This makes interpretation of the images difficult, and the only way to extract accurate structural information is to compare the experimental results to simulations.

A solution to the issues with CTEM arose in the 1980s with the development of the high-angle annular dark field (HAADF) detector in STEM. In STEM an electron beam is focused to a point and scanned across the sample; detectors below the sample then record the intensity at each point scanned to produce an image as shown in figure 4.5.[46] The bright field detector in a STEM lies on the optical axis and produces images that are equivalent to bright field CTEM images, though bright field STEM offers higher resolution.[47] Concurrently, the HAADF detector detects electrons that have scattered to larger angles and produces incoherent images where the intensity scales with the atomic number Z approximately as Z^2.[47] The incoherent nature of the HAADF images makes it possible to directly interpret the structural features of the images without simulations.

With the addition of aberration correctors, STEM has achieved sub-angstrom probe sizes which when combined with the HAADF detector allows the imaging of individual atomic columns.[48] Aberration correctors also allow for wider illumination angles to be used which reduces the depth of field. With typical convergence angles, information can be obtained from a region approximately 20 nm thick and the focal depth can be adjusted in steps of less than 1 nm.[48] This creates the possibility of defocusing the probe through a sample to optically section the sample as illustrated in figure 4.6.[49] This technique has allowed the positions of individual atoms to be determined with nanometer resolution with the only requirement being that the atoms of interest have a significantly larger atomic number than the surroundings.[48] It is important to note that defocusing the beam into the sample has a smaller step

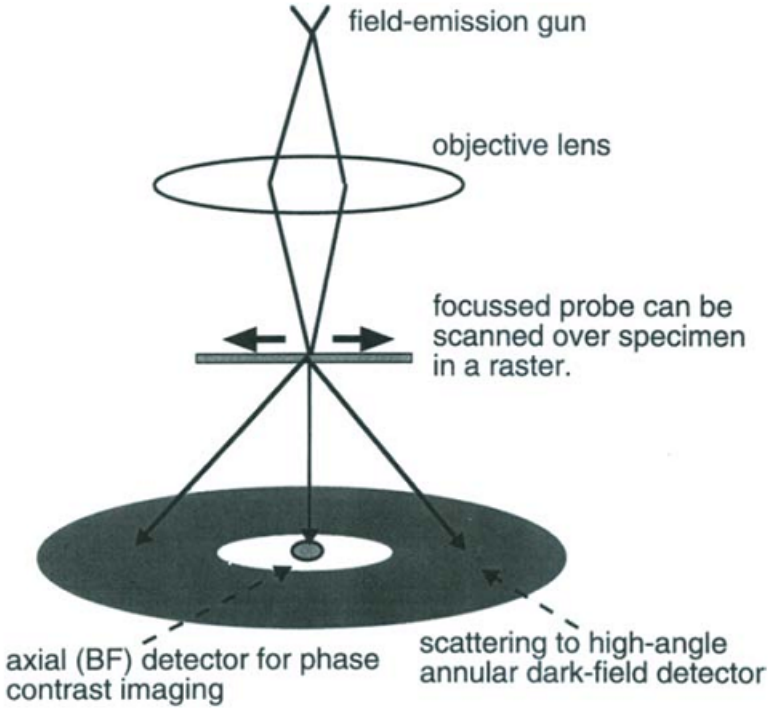

Figure 4.5: Illustration of STEM detectors.[46]

size than the depth of the volume probed. Thus, to determine the placement of a structure in the bulk of the specimen it is necessary to look for changes in a series of images.

Since the intensity of a HAADF image increases with Z, it can be used to identify regions of different atomic species and to estimate the composition of the individual atomic columns. This can be done by normalizing the integrated intensities in the region of interest to those of a reference layer. In a study of $InAs_xP_{1-x}$ it was found that the normalized integrated intensity increased linearly with As content of the material, and thus could be used to estimate the composition across an interface.[50]

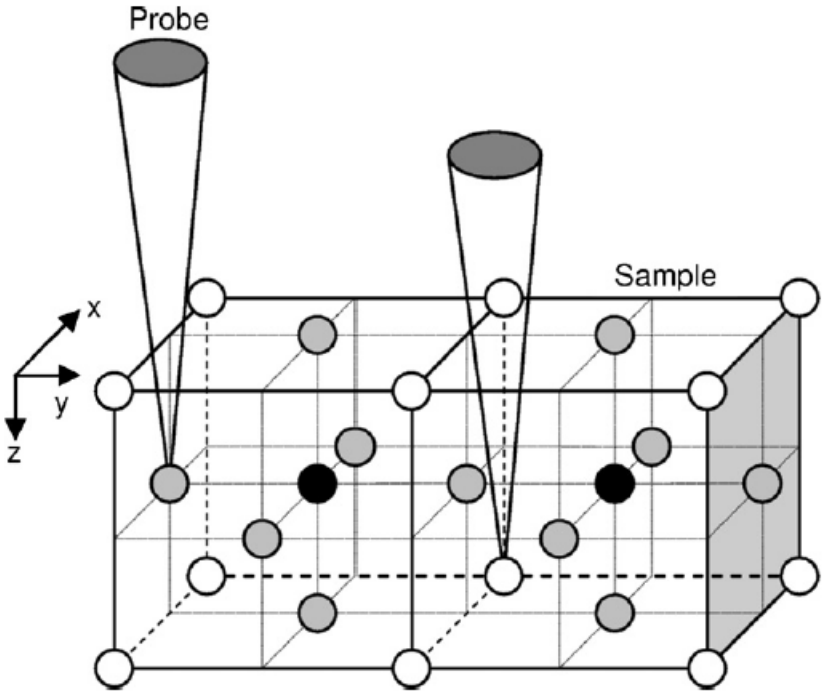

Figure 4.6: Illustration of the depth sectioning technique.[49]

4.3 Sample Preparation

In order for a sample to be studied by TEM, a piece of the sample must first be thinned to electron transparency. For high resolution work this means thinning it to less than 100 nm. There are a variety of methods for sample preparation that are well documented, and the material under investigation dictates which method is used. For this work, a method known as wedge polishing followed by Ar^+ ion milling was selected. Mechanical preparation was chosen for the sample since the purpose of this work was to study the composition of the sample, and the results could be compromised by implantation of Ga during preparation by FIB.

To produce a specimen for study, two 3 mm x 5 mm pieces where cut from the sample and placed together so that the two surfaces with the AlGaInN film faced each other with a piece of silicon that had been thinned to approximately 100 μm in between. This was then placed between two pieces of silicon to help provide

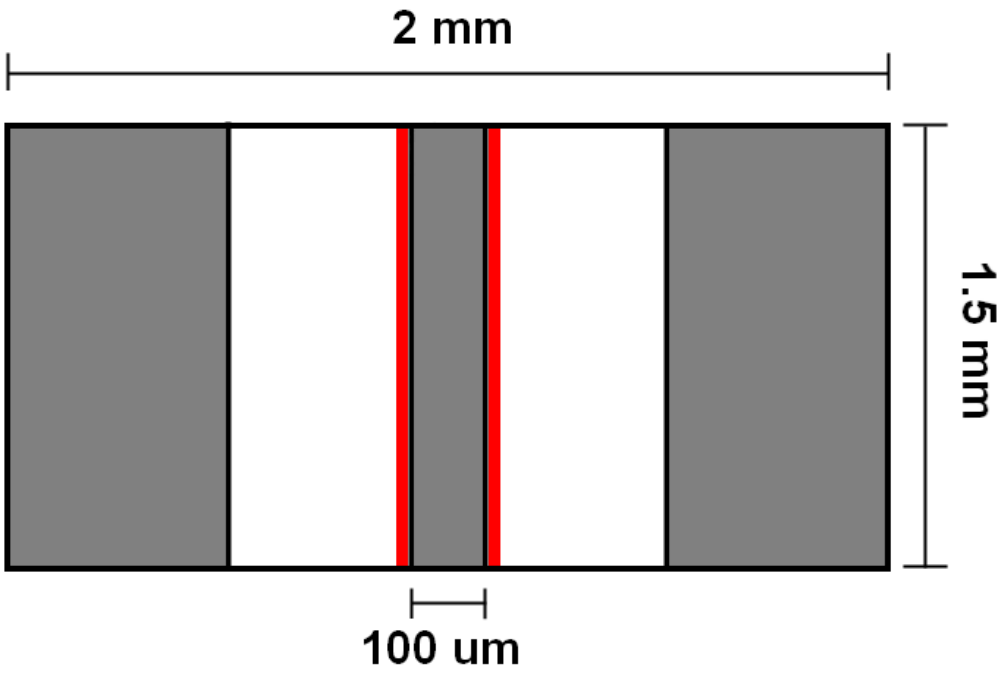

Figure 4.7: Illustration of the sandwich.

stability during polishing, and the entire structure bonded together using epoxy. This structure is illustrated in figure 4.7, where the gray areas are silicon, the white sapphire, and the red the film of interest.

A slice was then cut from this bulk sandwich which was then trimmed to length to give a piece approximately 2 mm x 1.5 mm x 1 mm. This piece was then mounted on a tripod polisher and polished using diamond lapping films with particle sizes of 30, 15, 6, 3, and 1 μm. After the first side was polished the sample was flipped, and the legs of the tripod adjusted to grind the sample into a wedge with an angle of about 1°. The same polishing sequence was then repeated while carefully monitoring the sample thickness using a micrometer. The center piece of silicon is used as a thickness indicator because at 20 μm silicon becomes translucent with a red hue. Once the silicon was seen to change color as shown in figure 4.8, polishing was stopped and the specimen was mounted to a grid.

The specimen and grid were then detached from the tripod polisher by soaking

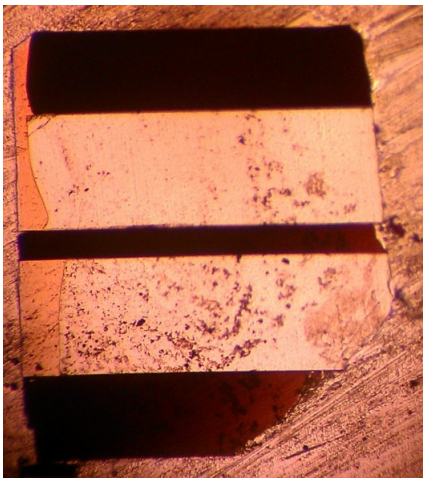

Figure 4.8: Specimen after polishing.

them in acetone. After drying, the final polishing of the sample was done using a Gatan Precision Ion Polishing System where Ar^+ ion milling was performed using a gun tilt of $\pm 5°$ and beam energies of 4.5 kV and 2 kV. The wedge polishing method used thinned the sample as much as possible to reduce the time used for ion milling which can heat the sample creating artifacts, or damage the sample by creating an amorphous layer which prevents high resolution imaging.

In addition to the sample reported on in this work, three other samples have been prepared using this method including another AlGaInN sample and two InAlN samples.

4.4 Results and Discussion

The AlGaInN sample studied in this work was grown at 750 °C on a (0001) sapphire substrate by MOCVD. The epistructure consists of 10 nm AlGaInN/1 nm AlN/1.9 μm GaN/20 nm AlGaN/sapphire substrate. The sample is estimated by IQE to contain 3-6% Ga and 14-17% In based on XRD and SIMS data from a sample grown using similar conditions.[51] The XRD measurements showed the AlGaInN peak separated from the GaN peak by 0.84 degrees, indicating the AlGaInN is not lattice matched to the buffer.[51]

A cross section sample for investigation by STEM was prepared along the $\langle 11\bar{2}0 \rangle$ zone axis using the procedure described in the previous section. Once the sample was prepared a series of depth sectioning images was collected using an aberration corrected JEOL JEM-ARM 200F operating at 200 kV by varying the depth at which the electron beam was focused in 1 nm steps from 0 nm at the focus starting point to +15 nm into the sample.

EDS measurements, shown in figure 4.9, confirmed the presence of Al, Ga, In, and N in the film. However, the film was seen to damage quickly under the electron beam, thus in order to prevent composition fluctuations from the damage a short dwell time was used resulting in the low number of counts.

To study the variation in composition, the atomic column intensities of the AlGaInN layer were normalized using the intensities of the GaN buffer layer for reference using the procedure described in Molina.[50] This was done to the images collected every 3 nm, and the results are shown in figure 4.10.[52] In these images the GaN buffer layer is seen at the top of the images, and the normalized intensities are overlaid on the AlGaInN below it.

For a sample of homogeneous thickness, intensity variations can be attributed to variations in atomic number. From the theoretical predictions the Al and Ga should be distributed randomly with only the In showing a tendency to form clusters.[28] Therefore, in the images shown in figure 4.10 the red regions, which mark the atomic columns with higher normalized intensity, are taken to be have higher In content relative to the other columns.

Thickness measurements by electron energy loss spectroscopy (EELS) show the sample to be 40 nm thick near the interface with the GaN buffer and decreasing to 30 nm in the AlGaInN layer. In the lateral direction, there was no appreciable change in thickness within the field of view. The intensity of HAADF contrast is a function of sample thickness. Therefore, this is likely the cause of the low intensity

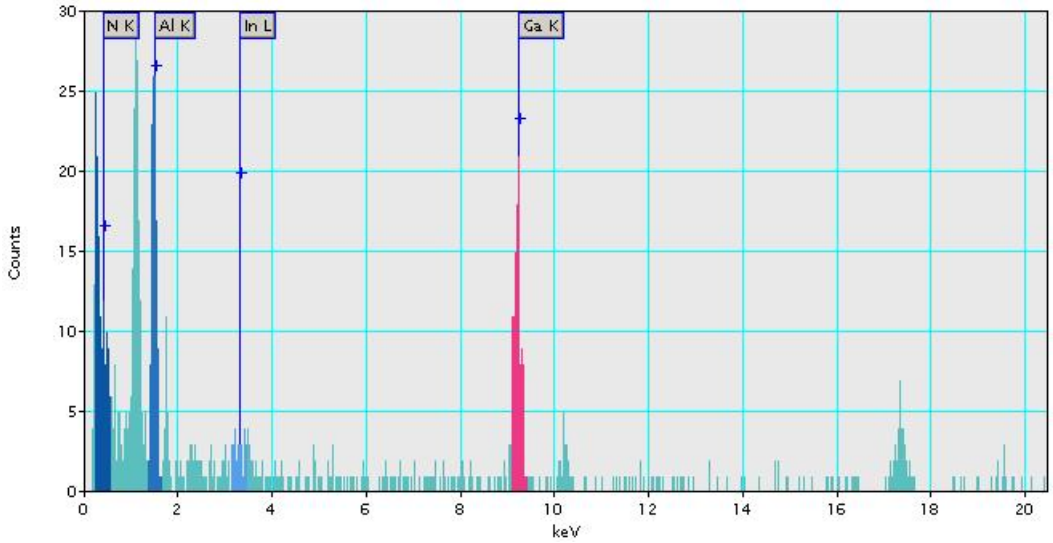

Figure 4.9: EDS line scan of the AlGaInN film.

regions, marked in light and dark blue in figure 4.10, near the bottom of the AlGaInN layer.

More care must be taken in interpreting the information from the focal series because the volume probed is larger than the step size so there is a common volume probed in each image. To account for this, it is necessary to look for regions in which the intensity changes between the images. One such region is marked in figure 4.10b. The intensity of this region is seen to steadily decrease throughout the series until it can no longer be distinguished from the surrounding area in figure 4.10f. Figure 4.11 shows an enlarged view of this region. The larger high intensity regions that remain consistent through out the focal series could either represent regions of high In content that extend through the sample, or could be caused by a more localized cluster in the volume common to the images in the focal series. In addition to these clusters of In, there also appears to be localized In content that is randomly distributed in the same manner as in an alloy.[52] This is seen in the region circled in figure 4.12 as individual columns of relatively high intensity that are separate from the larger clusters.

Unfortunately, quantification of the composition for this sample proved to be

impossible. EDS measurements lack the spatial resolution to determine where the signal is originating. It is possible to measure the composition with atomic resolution using EELS, but the available spectrometer lacked the spatial resolution to do so. The accuracy of the quantification using the normalized intensities has recently come into question for materials with two elements, and thus is unreliable for this material with its four elements.[53]

The number of variables involved also made simulations unfeasible because while the HAADF images are incoherent in directions perpendicular to the beam, coherence effects arise within the columns of atoms.[46] This means factors such as the sample thickness, which was seen to vary, and the order of the atoms in the column can effect the observed intensity.[54] It is also possible that the intensity of a column can be influenced by the columns surrounding it.[55]

In summary, theoretical predictions using the regular solution model show that phase separation via spinodal decomposition should occur in the AlGaInN sample studied. This has been confirmed by other calculations which have shown that it is only the In that tends to form clusters.[28] In the HAADF images the regions with the highest relative intensities were observed to be clustered together which is consistent with the formation of In clusters. From this it can be concluded that there is evidence of phase separation in the AlGaInN that is the result of spinodal decomposition.

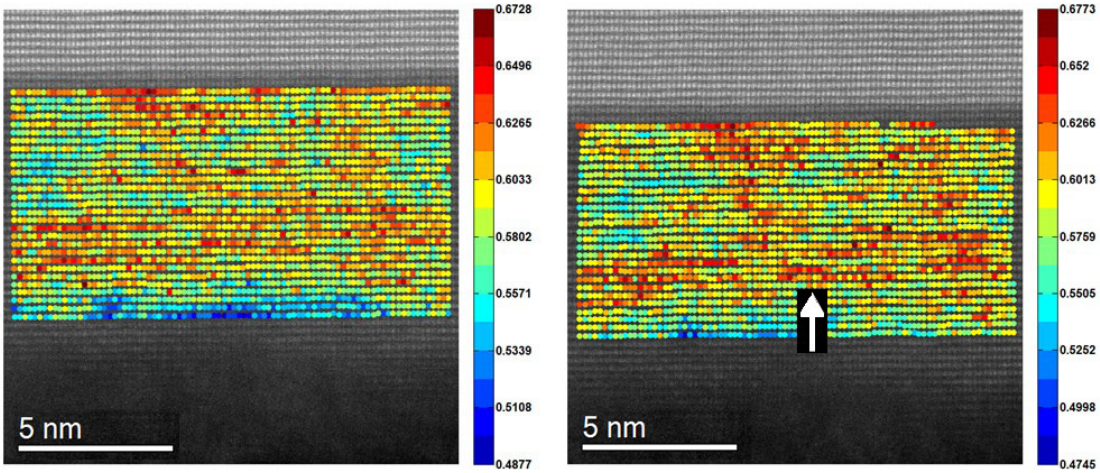

(a) $\Delta f = 0$ nm (b) $\Delta f = +3$ nm

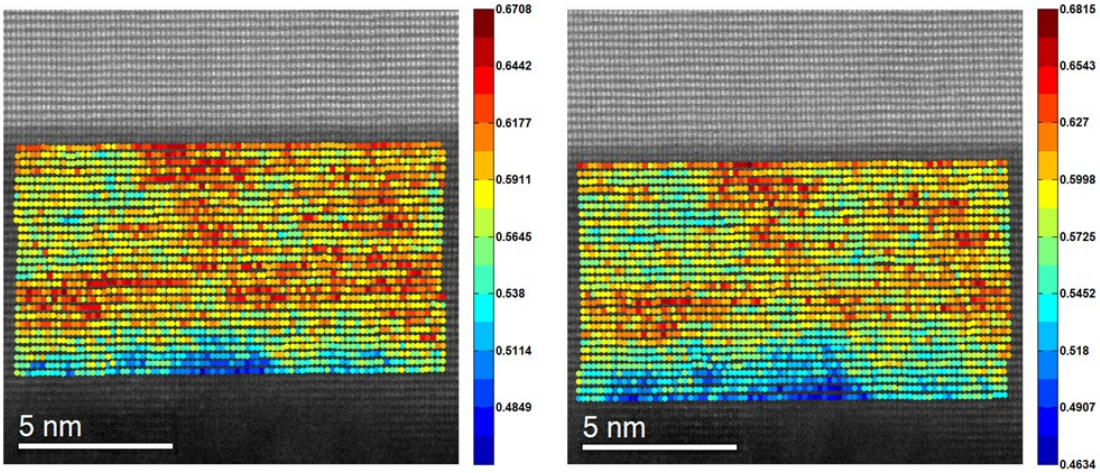

(c) $\Delta f = +6$ nm (d) $\Delta f = +9$ nm

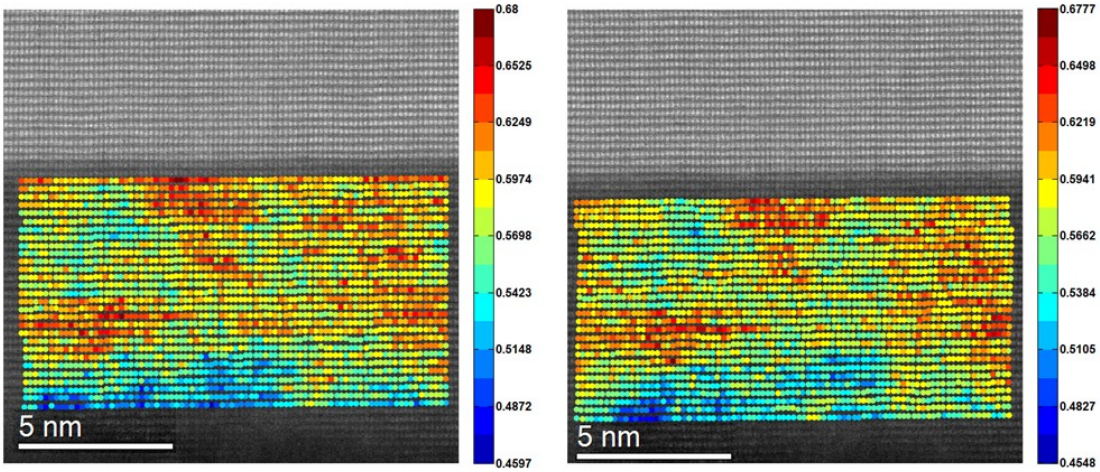

(e) $\Delta f = +12$ nm (f) $\Delta f = +15$ nm

Figure 4.10: Integrated intensities overlayed on HAADF images.

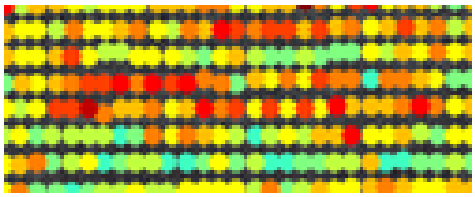

(a) $\Delta f = +3$ nm

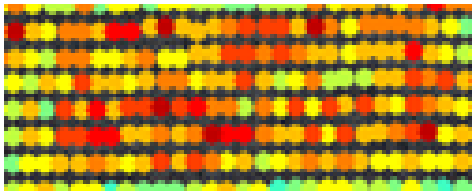

(b) $\Delta f = +6$ nm

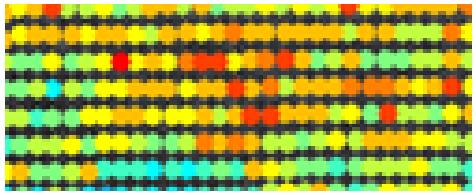

(c) $\Delta f = +9$ nm

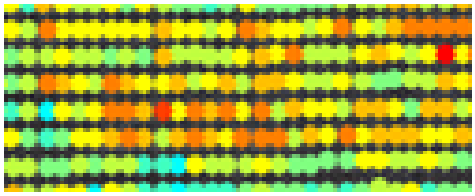

(d) $\Delta f = +12$ nm

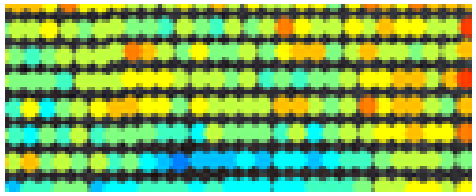

(e) $\Delta f = +15$ nm

Figure 4.11: Detail view of the region marked in figure 4.10b.

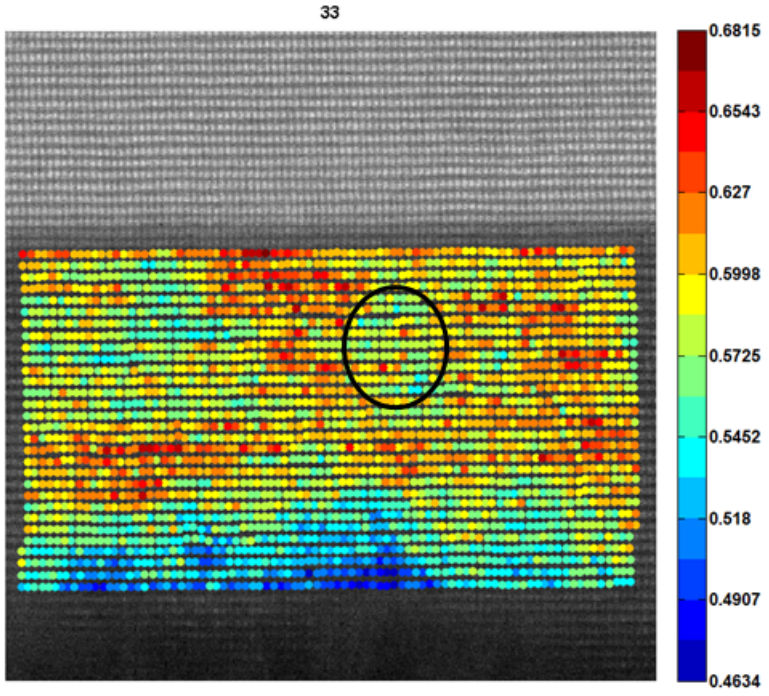

Figure 4.12: Evidence of randomly distributed In content.

CHAPTER 5

Conclusions and Future Work

5.1 Reactor

At this point the oxygen contamination issues have been successfully addressed, and general parameters for the deposition of AlN, GaN, and AlGaN have been established. The next major goal should be to produce device quality material using this work as a foundation.

The first step towards this goal is to improve the flow conditions within the chamber to reduce the number of particles landing on the surface during deposition, and creating some region of consistent AlGaN composition. Accomplishing this will require replacing the substrate heater, and possibly more extensive modifications, if not complete replacement, of the chamber body. Once these issues have been addressed, the next major step is to tune the growth conditions for the transition layers to produce a crack-free GaN buffer layer.

In the longer term, modifications need to be made to the reactor to include lines for dopants, and growth processes developed for In containing alloys.

5.2 AlGaInN

As mentioned, three more specimens have been prepared for study by STEM. One is a 65 nm thick AlGaInN sample with composition similar to the one studied in this work, and the other two are InAlN with In contents similar to the quaternary samples that are 10 nm and 70 nm thick.

Since the quaternary is not lattice matched to the GaN buffer, the lattice of the 10 nm sample is likely pseudomorphic to the buffer layer. Thus, comparison of the two quaternary samples could give insight into how stress and growth time affect

the composition of the film. By comparing the InAlN and quaternary samples, it should be possible to see how the presence of Ga influences the distribution of In within the material.

REFERENCES

[1] A. C. Jones and M. L. Hitchman, eds., *Chemical Vapour Deposition: Precursors, Processes and Applications*, 1st ed. (Royal Society of Chemistry, 2008).

[2] G. B. Stringfellow, *Organometallic Vapor-Phase Epitaxy: Theory and Practice*, 2nd ed. (Academic Press, 1999).

[3] Z. Alferov, Semiconductors **32**, 1 (1998).

[4] S. Strite and H. Morkoç, Journal of Vacuum Science & Technology B **10**, 1237 (1992).

[5] H. P. Maruska and J. J. Tietjen, Applied Physics Letters **15** (1969).

[6] H. M. Manasevit, F. M. Erdmann, and W. I. Simpson, Journal Electrochemical Society **118**, 1864 (1971).

[7] V. Davydov, A. Klochikhin, R. Seisyan, V. Emtsev, S. Ivanov, F. Bechstedt, J. Furthmller, H. Harima, A. Mudryi, J. Aderhold, O. Semchinova, and J. Graul, Physica Status Solidi B **229**, R1 (2002).

[8] D. Zhu, D. J. Wallis, and C. J. Humphreys, Reports on Progress in Physics **76**, 106501 (2013).

[9] G. Ariyawansa, M. B. M. Rinzan, M. Alevli, M. Strassburg, N. Dietz, A. G. U. Perera, S. G. Matsik, A. Asghar, I. T. Ferguson, H. Luo, A. Bezinger, and H. C. Liu, Applied Physics Letters **89**, 091113 (2006).

[10] N. Lu and I. Ferguson, Semiconductor Science and Technology **28**, 074023 (2013).

[11] H. Amano, N. Sawaki, I. Akasaki, and Y. Toyoda, Applied Physics Letters **48**, 353 (1986).

[12] H. Amano, M. Kito, K. Hiramatsu, and I. Akasaki, Japanese Journal of Applied Physics **28**, L2112 (1989).

[13] T. Matsuoka, N. Yoshimoto, T. Sasaki, and A. Katsui, Journal of Electronic Materials **21**, 157 (1992).

[14] F. G. McIntosh, K. S. Boutros, J. C. Roberts, S. M. Bedair, E. L. Piner, and N. A. El-Masry, Applied Physics Letters **68**, 40 (1996).

[15] I. Ho and G. Stringfellow, Applied Physics Letters **69**, 2701 (1996).

[16] N. A. El-Masry, E. L. Piner, S. X. Liu, and S. M. Bedair, Applied Physics Letters **72**, 40 (1998).

[17] T. Matsuoka, Journal of Crystal Growth **190**, 19 (1998).

[18] T. Takayama, M. Yuri, K. Itoh, T. Baba, and J. Harris Jr, Journal of Crystal Growth **222**, 29 (2001).

[19] A. Chitnis, A. Kumar, M. Shatalov, V. Adivarahan, A. Lunev, J. W. Yang, G. Simin, M. A. Khan, R. Gaska, and M. Shur, Applied Physics Letters **77**, 3800 (2000).

[20] O. Ambacher, J. Smart, J. R. Shealy, N. G. Weimann, K. Chu, M. Murphy, W. J. Schaff, L. F. Eastman, R. Dimitrov, L. Wittmer, M. Stutzmann, W. Rieger, and J. Hilsenbeck, Journal of Applied Physics **85** (1999).

[21] J. Kuzmik, IEEE Electron Device Letters **22**, 510 (2001).

[22] A. Lobanova, A. Segal, E. Yakovlev, and R. Talalaev, Journal of Crystal Growth **352**, 199 (2012).

[23] J. Zhang, J. Yang, G. Simin, M. Shatalov, M. A. Khan, M. S. Shur, and R. Gaska, Applied Physics Letters **77**, 2668 (2000).

[24] H. Hirayama, A. Kinoshita, T. Yamabi, Y. Enomoto, A. Hirata, T. Araki, Y. Nanishi, and Y. Aoyagi, Applied Physics Letters **80**, 207 (2002).

[25] V. Adivarahan, A. Chitnis, J. P. Zhang, M. Shatalov, J. W. Yang, G. Simin, M. A. Khan, R. Gaska, and M. S. Shur, Applied Physics Letters **79**, 4240 (2001).

[26] M. A. Khan, V. Adivarahan, J. P. Zhang, C. Chen, E. Kuokstis, A. Chitnis, M. Shatalov, J. W. Yang, and G. Simin, **40**, 1308 (2001).

[27] G. Kipshidze, V. Kuryatkov, B. Borisov, M. Holtz, S. Nikishin, and H. Temkin, Applied Physics Letters **80**, 3682 (2002).

[28] M. Marques, L. Teles, L. Scolfaro, L. Ferreira, and J. Leite, Physical Review B **70**, 073202 (2004).

[29] J. Wu, J. Li, G. Cong, H. Wei, P. Zhang, W. Hu, X. Liu, Q. Zhu, Z. Wang, Q. Jia, and L. Guo, Nanotechnology **17**, 1251 (2006).

[30] Y. Liu, T. Egawa, H. Jiang, B. Zhang, H. Ishikawa, and M. Hao, Applied Physics Letters **85**, 6030 (2004).

[31] Y. Liu, H. Jiang, S. Arulkumaran, T. Egawa, B. Zhang, and H. Ishikawa, Applied Physics Letters **86**, 223510 (2005).

[32] L. R. Khoshroo, C. Mauder, H. Behmenburg, J. Woitok, W. Zander, J. Gruis, B. Reuters, J. Schubert, A. Vescan, M. Heuken, H. Kalisch, and R. H. Jansen, Physica Status Solidi C **6**, S470 (2009).

[33] T. Lim, R. Aidam, P. Waltereit, T. Henkel, R. Quay, R. Lozar, T. Maier, L. Kirste, and O. Ambacher, IEEE Electron Device Letters **31**, 671 (2010).

[34] F. Lecourt, A. Agboton, N. Ketteniss, H. Behmenburg, N. Defrance, V. Hoel, H. Kalisch, A. Vescan, M. Heuken, and J. C. de Jaeger, IEEE Electron Device Letters **34**, 978 (2013).

[35] R. Wang, G. Li, G. Karbasian, J. Guo, B. Song, Y. Yue, Z. Hu, O. Laboutin, Y. Cao, W. Johnson, G. Snider, P. Fay, D. Jena, and H. G. Xing, IEEE Electron Device Letters **34**, 378 (2013).

[36] E. L. Piner, M. K. Behbehani, N. A. El-Masry, F. G. McIntosh, J. C. Roberts, K. S. Boutros, and S. M. Bedair, Applied Physics Letters **70**, 461 (1997).

[37] Y. Fujikawa, Y. Yamada-Takamura, G. Yoshikawa, T. Ono, M. Esashi, P. P. Zhang, M. G. Lagally, and T. Sakurai, Applied Physics Letters **90**, 243107 (2007).

[38] J. Chung, J. kyu Lee, E. Piner, and T. Palacios, Electron Device Letters, IEEE **30**, 1015 (2009).

[39] C. Huang, S. Chang, R. Chuang, J. Lin, Y. Cheng, and W. Lin, Applied Surface Science **256**, 6367 (2010).

[40] A. Able, W. Wegscheider, K. Engl, and J. Zweck, Journal of Crystal Growth **276**, 415 (2005).

[41] H. Habuka, H. Tsunoda, M. Mayusumi, N. Tate, and M. Katayama, Journal of the Electrochemcial Society **142**, 3092 (1995).

[42] A. Dadgar, A. Krost, J. Christen, B. Bastek, F. Bertram, A. Krtschil, T. Hempel, J. Blsing, U. Haboeck, and A. Hoffmann, Journal of Crystal Growth **297**, 306 (2006).

[43] H. Lahreche, P. Vennegues, O. Tottereau, M. Laugt, P. Lorenzini, M. Leroux, B. Beaumont, and P. Gibart, Journal of Crystal Growth **217**, 13 (2000).

[44] D. R. Gaskell, *Introduction to the Thermodynamics of Materials*, 5th ed. (Taylor & Francis, 2008).

[45] D. A. Porter and K. E. Easterling, *Phase Transformations in Metals and Alloys*, 2nd ed. (Chapman & Hall, 1992).

[46] P. Nellist and S. Pennycook, in *Advances in Imaging and Electron Physics*, Vol. 113, edited by P. W. Hawkes (Elsevier, 2000) pp. 147 – 203.

[47] S. J. Pennycook and P. D. Nellist, eds., *Scanning Transmission Electron Microscopy Imaging and Analysis* (Springer, 2011).

[48] K. van Benthem, A. R. Lupini, M. P. Oxley, S. D. Findlay, L. J. Allen, and S. J. Pennycook, Ultramicroscopy **106**, 1062 (2006).

[49] A. DAlfonso, S. Findlay, M. Oxley, S. Pennycook, K. van Benthem, and L. Allen, Ultramicroscopy **108**, 17 (2007).

[50] S. Molina, D. Sales, P. Galindo, D. Fuster, Y. González, B. Alén, L. González, M. Varela, and S. Pennycook, Ultramicroscopy **109**, 172 (2009).

[51] O. Labutin and W. Johnson, Personal Communication.

[52] J. W. Anderson, F. Ruiz, O. Laboutin, Y. Cao, A. Ponce, J. W. Johnson, and E. L. Piner, In Preparation.

[53] A. Ponce, Personal Communication.

[54] H. L. Xin, V. Intaraprasonk, and D. A. Muller, Applied Physics Letters **92**, 013125 (2008).

[55] W. V. den Broek, S. V. Aert, and D. V. Dyck, Ultramicroscopy **110**, 548 (2010).

[56] T. G. Zhu, D. J. H. Lambert, B. S. Shelton, M. M. Wong, U. Chowdhury, and R. D. Dupuis, Applied Physics Letters **77**, 2918 (2000).